Supporting information for:

---

*Generating potent C-H PCET donors: Ligand-induced Fe-to-ring proton migration from a Cp*Fe^{III}-H complex demonstrates a promising strategy*

*Dirk J. Schild†, Marcus W. Drover†, Paul H. Oyala, and Jonas C. Peters**

Division of Chemistry and Chemical Engineering, California Institute of Technology, Pasadena, California 91125, United States

† These authors contributed equally

*E-mail: jpeters@caltech.edu

1. General Considerations

All experiments were carried out employing standard Schlenk techniques under an atmosphere of dry nitrogen or argon employing degassed, dried solvents in a solvent purification system supplied by SG Water, LLC. Non-halogenated solvents were tested with a standard purple solution of sodium benzophenone ketyl in tetrahydrofuran to confirm effective moisture removal. $Fe^{II}(\eta^5\text{-}Cp^*)(dppe)X$ (X = Cl, H, CH_3, OTf)[1] were prepared according to a literature procedure. All other reagents were purchased from commercial vendors and used without further purification unless otherwise stated.

1.1. Nuclear Magnetic Resonance Spectroscopy

^1H and ^{13}C chemical shifts are reported in ppm relative to tetramethylsilane, using residual solvent resonances as internal standards. ^{31}P chemical shifts are reported in ppm and referenced externally to 85% aqueous H_3PO_4 at 0 ppm.

1.2. ^{57}Fe Mössbauer Spectroscopy

Mössbauer spectra were recorded on a spectrometer from SEE Co. (Edina, MN) operating in the constant acceleration mode in transmission geometry. The sample was kept in an SVT-400 cryostat form Janis (Wilmington, MA), using liquid N_2 as a cryogen for 80 K measurements. The quoted isomer shifts are relative to the centroid of the spectrum of a metallic foil of α-Fe at room temperature. Solid samples were prepared by grinding solid material into a fine powder and then mounted in to a Delrin cup fitted with a screw cap as a boron nitride pellet. Solution samples were transferred to a sample cup and chilled to 77 K inside of the glovebox, and quickly removed from the glovebox and immersed in liquid N_2 until mounted in the cryostat. Data analysis was performed using WMOSS version 4 (www.wmoss.org) and quadrupole doublets were fit to Lorentzian lineshapes.[2]

1.3. Infrared Spectroscopy

Solid and thin film IR measurements were obtained on a Bruker Alpha spectrometer equipped with a diamond ATR probe.

1.4. UV-VIS Spectroscopy

UV-Visible spectroscopy measurements were collected with a Cary 50 UV-Vis spectrophotometer using a 1 cm two-window quartz cell.

1.5. EPR Spectroscopy

Continuous wave X-band EPR spectra were obtained on a Bruker EMX spectrometer on 2-9 mM solutions prepared as frozen glasses in 2-MeTHF. Pulse EPR spectroscopy: All pulse X-band (9.4-9.7 GHz) EPR, electron nuclear double resonance (ENDOR), and hyperfine sublevel correlation spectroscopy (HYSCORE) experiments were acquired using a Bruker ELEXSYS E580 pulse EPR spectrometer. X-band ENDOR experiments were performed using a Bruker MD-4 X-band ENDOR resonator, and X-band HYSCORE experiments were performed using a Bruker MS-5 resonator. Temperature control was achieved using an ER 4118HV-CF5-L Flexline Cryogen-Free VT cryostat manufactured by ColdEdge equipped with an Oxford Instruments Mercury ITC temperature controller.

All pulse X-band ($\nu \approx 9.4$-9.7 GHz) EPR and electron nuclear double resonance (ENDOR) experiments were aquired using a Bruker (Billerica, MA) ELEXSYS E580 pulse EPR spectrometer equipped with a Bruker MD-4 resonator. Temperature control was achieved using an ER 4118HV-CF5-L Flexline Cryogen-Free VT cryostat manufactured by ColdEdge (Allentown, PA) equipped with an Oxford Instruments Mercury ITC.

Pulse X-band ENDOR was acquired using the Davies pulse sequence ($\pi - T_{RF} - \pi_{RF} - T_{RF} - \pi/2 - \tau - \pi -$ echo), where T_{RF} is the delay between mw pulses and RF pulses, π_{RF} is the length of the RF pulse and the RF frequency is randomly sampled during each pulse sequence.

X-band HYSCORE spectra were acquired using the 4-pulse sequence ($\pi/2 - \tau - \pi/2 - t_1 - \pi - t_2 - \pi/2 -$ echo), where τ is a fixed delay, while t_1 and t_2 are independently incremented by Δt_1 and Δt_2, respectively. The time domain data was baseline-corrected (third-order polynomial) to eliminate the exponential decay in the echo intensity, apodized with a Hamming window function, zero-filled to eight-fold points, and fast Fourier-transformed to yield the 2-dimensional frequency domain. For ^{2}H-^{1}H difference spectra, the time domain of the HYSCORE spectrum of the ^{1}H sample was subtracted from that of the ^{2}H sample, and the same data processing procedure detailed above was used to generate the frequency spectrum.

In general, the ENDOR spectrum for a given nucleus with spin I= ½ (^{1}H, ^{31}P) coupled to the S = ½ electron spin exhibits a doublet at frequencies

$$\nu_{\pm} = \left|\frac{A}{2} \pm \nu_N\right| \quad (1)$$

Where ν_N is the nuclear Larmor frequency and A is the hyperfine coupling. For nuclei with $I \geq 1$ (^{2}H), an additonal splitting of the $\nu_{\pm}$ manifolds is produced by the nuclear quadrupole interaction (P)

$$\nu_{\pm,m_I} = \left|\nu_N \pm \frac{3P(2m_I - 1)}{2}\right| \quad (2)$$

In HYSCORE spectra, these signals manifest as cross-peaks or ridges in the 2-D frequency spectrum which are generally symmetric about the diagonal of a given quadrant. This technique allows hyperfine levels corresponding to the same electron-nuclear submanifold to be differentiated, as well as separating features from hyperfine couplings in the weak-coupling regime ($|A| < 2|\nu_I|$) in the (+,+) quadrant from those in the strong coupling regime ($|A| > 2|\nu_I|$) in the (−,+) quadrant. The (−,−) and (+,−) quadrants of these frequency spectra are symmetric to the (+,+) and (−,+) quadrants, thus typically only two of the quadrants are displayed in literature.

For systems with appreciable hyperfine anisotropy in frozen solutions or solids, HYSCORE spectra typically do not exhibit sharp cross peaks, but show ridges that represent the sum of cross peaks from selected orientations within the excitation bandwidth of the MW pulses at the magnetic field position at which the spectrum is collected. The length and curvature of these correlation ridges can allow for the separation and estimation of the magnitude of the isotropic and dipolar components of the hyperfine tensor, as shown in Fig. S1.

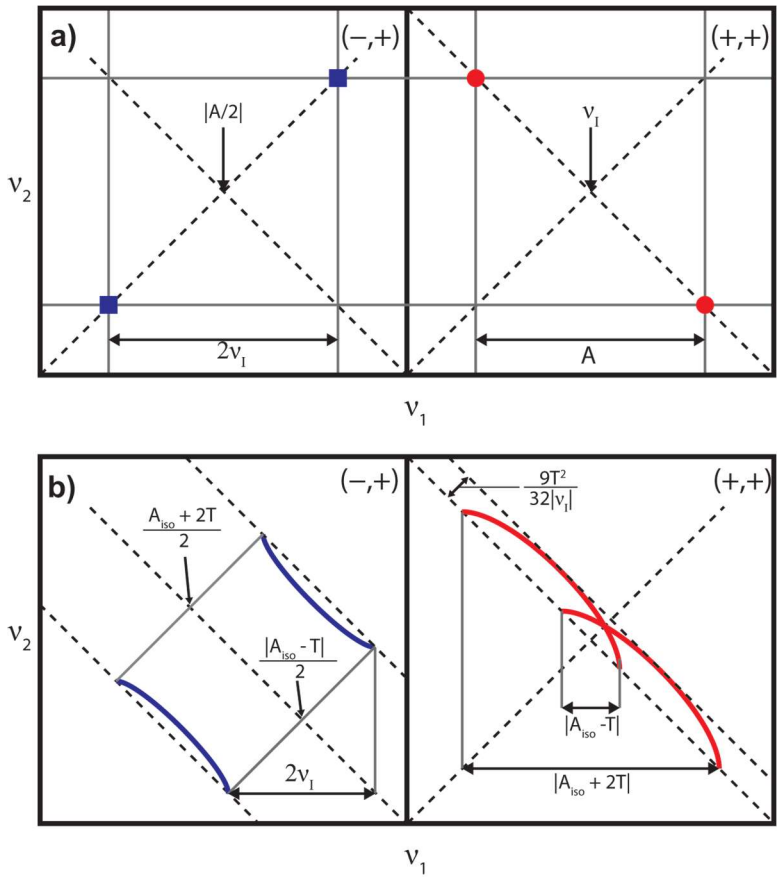

Figure S1. a) HYSCORE powder patterns for an S = 1/2, I = 1/2 spin system with an isotropic hyperfine tensor A. b) HYSCORE powder patterns for an S = 1/2, I = 1/2 spin system with an axial hyperfine tensor which contains isotropic (a_{iso}) and dipolar (T) contributions. Blue correlation ridges represent the strong coupling case; red correlation ridges represent the weak coupling case.

EPR Simulations. Simulations of all CW and pulse EPR data were achieved using the EasySpin[3] simulation toolbox (release 5.2.21) with Matlab 2018b using the following Hamiltonian:

$$\hat{H} = \mu_B \vec{B}_0 g \hat{S} + \mu_N g_N \vec{B}_0 \hat{I} + h\hat{S} \cdot \mathbf{A} \cdot \hat{I} + h\hat{I} \cdot \mathbf{P} \cdot \hat{I} \qquad (3)$$

In this expression, the first term corresponds to the electron Zeeman interaction term where μ_B is the Bohr magneton, g is the electron spin g-value matrix with principle components g = [g_{xx} g_{yy} g_{zz}], and $\hat{S}$ is the electron spin operator; the second term corresponds to the nuclear Zeeman interaction term where μ_N is the nuclear magneton, g_N is the characteristic nuclear g-value for each nucleus (e.g. ^{1}H, ^{2}H ,^{31}P) and $\hat{I}$ is the nuclear spin operator; the third term corresponds to the electron-nuclear hyperfine term, where **A** is the

hyperfine coupling tensor with principle components **A** = [A_{xx}, A_{yy}, A_{zz}]; and for nuclei with $I \geq 1$, the final term corresponds to the nuclear quadrupole (NQI) term which arises from the interaction of the nuclear quadrupole moment with the local electric field gradient (efg) at the nucleus, where **P** is the quadrupole coupling tensor. In the principle axis system (PAS), **P** is traceless and parameterized by the quadrupole coupling constant e^2Qq/h and the asymmetry parameter η such that:

$$\mathbf{P} = \begin{pmatrix} P_{xx} & 0 & 0 \\ 0 & P_{yy} & 0 \\ 0 & 0 & P_{zz} \end{pmatrix} = \frac{e^2Qq/h}{4I(2I-1)} \begin{pmatrix} -(1-\eta) & 0 & 0 \\ 0 & -(1+\eta) & 0 \\ 0 & 0 & 2 \end{pmatrix} \quad (4)$$

where $\frac{e^2Qq}{h} = 2I(2I-1)P_{zz}$ and $\eta = \frac{P_{xx}-P_{yy}}{P_{zz}}$. The asymmetry parameter may have values between 0 and 1, with 0 corresponding to an electric field gradient with axial symmetry and 1 corresponding to a fully rhombic efg.

The orientations between the hyperfine and NQI tensor principle axis systems and the g-matrix reference frame are defined by the Euler angles (α, β, γ).

1.6. Electrochemistry

Electrochemical measurements were carried out using a CD instruments 600B electrochemical analyzer. A freshly polished glassy carbon electrode was used as the working electrode and a graphite rod was used as the auxiliary electrode. Solutions (THF) of electrolyte (0.4 M tetra-n-butylammonium hexafluorophosphate) contained ferrocene (0.1 mM), to serve as an internal reference, and analyte (0.2 mM). All reported potentials are referenced to the ferrocene/ferrocenium couple, $[Cp_2Fe]^+$ /Cp_2Fe.

2. Synthetic Procedures

[Fe^{III}(η^5-Cp*)(dppe)H]BAr$^{F}_4$ ([**1**]BAr$^{F}_4$: $C_{68}H_{52}BF_{24}FeP_2$; 1453.3 gmol^{-1}): To a solution of **Fe^{II}(η^5-Cp*)(dppe)H** (40 mg, 0.07 mmol, 1 equiv.) in Et_2O (2 mL) at -78 °C was added an Et_2O (2 mL) solution of [Fc]BAr$^{F}_4$ (60 mg, 0.06 mmol, 0.85 equiv.). Following addition, the resulting dark orange mixture was stirred at 25 °C over 10 min giving a dark red-orange solution. Removal of volatiles *in-vacuo* and washing with pentane gave [**1**]BAr$^{F}_4$ as a red solid (72 mg, 74%). ***N.B.*** The PF_6^- salt has been prepared previously, though ^{1}H NMR data was not provided.[4] **^{1}H NMR (THF-d$_8$, 400 MHz, 298 K)**:δ = 54.12 (br), 26.46 (br), 9.88 (br), 8.71 (br), 7.80 (BAr$^{F}_4$), 7.58 (BAr$^{F}_4$), 7.40 (br), 5.61 (br), -0.15 (br), -2.51 (br), -9.00 (br).

Fe(*endo*–η^4-Cp*H)(dppe)(CO) (*endo*-**3**): Prepared as previously reported.[5] The solid-state molecular structure was not reported and is shown in the crystallography section. **UV-VIS (THF, nm {cm^{-1} M^{-1})**: 450 {1130}. **IR (ATR, C$_6$D$_6$ film)**: 1864 cm^{-1} (νCO).

[Fe(*endo*–η^4-Cp*H)(dppe)(CO)]BAr$^{F}_4$ (*endo*-[**3**]BAr$^{F}_4$): To a solution of [**1**]BAr$^{F}_4$ (10 mg, 0.007 mmol) in 2-MeTHF (2 mL) at -78 °C was added CO (~1 atm) in a J. Young EPR tube, giving a green solution. CW X-band EPR spectroscopy evidenced complete consumption of the Fe^{III}-H starting material. **UV-VIS (THF, nm {cm^{-1} M^{-1})**: 891 {252}, 712 {425}, 459 {870}, 383 {1530}. **EPR Parameters (30 K, 2-MeTHF, 9.717 GHz):** g = [2.085, 2.039, 2.004]; A(^{31}P$_1$) = [72, 59, 58] MHz; A(^{31}P$_2$) = [49, 42, 51] MHz; A(^{1}H) = ± [24, 20, 34.5] MHz.

Fe(*exo*–η^4-Cp*H)(dppe)(CO) (*exo*-**3**): To a solution of [Fe(η^5-Cp*)(dppe)CO]OTf (229.9 mg, 0.3 mmol, 1 equiv.) in Et_2O (20 mL) at -78 °C was added drop-wise a solution of 1 M $LiBEt_3H$ in Et_2O (0.3 mL, 0.3 mmol, 1 equiv. Following addition, the resulting mixture was stirred at 25 °C over 10 min giving a clear yellow solution. Volatiles were removed *in-vacuo* and the sample was extracted with 200 mL pentane, and filtered over celite. Removal of pentane *in-vacuo* yields *exo*-**3** as a yellow solid (158 mg, 85%). X-ray quality crystals are formed by cooling down a concentrated pentane solution of *exo*-**3** to -35 °C. **^{1}H NMR (400 MHz, C$_6$D$_6$)**: δ = 7.91 (t, $^3J_{H,H}$ = 8.2 Hz, 4H), 7.33 (h, $^3J_{H,H}$ = 3.8, 2.9 Hz, 4H), 7.27 – 7.18 (m, 4H), 7.14 – 7.03 (m, 8H), 3.04 (q, $^3J_{H,H}$ = 6.8 Hz, 1H), 2.23 – 2.01 (m, 2H), 1.83 (q, $^3J_{H,H}$ = 2.2 Hz, 9H), 1.65 (td, $^3J_{H,H}$ = 15.7, 12.7, 6.8 Hz, 2H), 0.97 (s, 6H), **^{13}C NMR (101 MHz, THF-d$_8$)**: δ = 139.7 – 138.8 (m), 138.3 (d, J = 16.8 Hz), 133.8 (t, J = 6.0 Hz), 133.1 (d, J = 5.3 Hz), 128.6 (d, J = 27.6 Hz), 127.3 (dt, J = 11.6, 4.1 Hz), 92.3, 60.8, 58.1, 31.0 – 29.9 (m), 13.1, 11.3. **^{31}P NMR (162 MHz, C$_6$D$_6$)**: δ = 85.3. **UV-VIS (THF, nm {cm^{-1} M^{-1})**: 441 {1850}. **IR (ATR, C$_6$D$_6$ film)**: 2711 cm^{-1} (νC–H), 2612 cm^{-1} (νC–H), 1854 cm^{-1} (νCO).

[Fe(*exo*-η^4-Cp*H)(dppe)(CO)]BAr$^{F}_4$ (*exo*-[**3**]BAr$^{F}_4$): In an 4 mm EPR tube, a frozen solution of *exo*-**3** (1.3 mg, 0.002 mmol) in 2-MeTHF (0.25 mL) was layered with a frozen solution of [Fc]BAr$^{F}_4$ (2.2 mg, 0.002 mmol, 1 equiv) in 0.25 mL 2-MeTHF. The two frozen solutions where slow thawed and stirred with a needle by taking the tube out of a cold well cooled with liquid nitrogen. Upon mixing, a color change to green can be observed. CW X-band EPR spectroscopy evidenced complete consumption of the Fe^{III}-H starting material. **UV-VIS (THF, nm {cm^{-1} M^{-1})**: 923 {130}, 767 {180}, 441 {1645}. **EPR Parameters (30 K, 2-MeTHF, 9.717 GHz):** g = [2.116, 2.073, 1.997]; A(^{31}P$_1$) = [96, 88, 47] MHz; A(^{31}P$_2$) = [78, 75, 63] MHz; A(^{1}H) = ± [85, 84, 83] MHz, HStrain = [70, 22, 22] MHz for conformer **A** (0.6 weight) and g = [2.093, 2.045, 2.013]; A(^{31}P$_1$) = [46, 44, 15] MHz; A(^{31}P$_2$) = [70, 64, 64] MHz; A(^{1}H) = ± [76, 74, 70] MHz, HStrain = [70, 22, 22] MHz for conformer **B** (0.4 weight).

[Fe(*endo*-η^4-Cp*H)(dppe)(CNXyl)]BAr$^{F}_4$ (*endo*-[**4**]BAr$^{F}_4$): To a solution of [**1**]BAr$^{F}_4$ (10 mg, 0.007 mmol) in 2-MeTHF (2 mL) at -78 ˚C was added CNXyl (~1 mg, 0.008 mmol, ~1.1 equiv.), giving a green solution. CW X-band EPR spectroscopy evidenced complete consumption of the Fe^{III}-H starting material. **UV-VIS (THF, nm):** 828. **EPR Parameters (20 K, 2-MeTHF, 9.716 GHz):** g = [2.132, 2.042, 2.004]; A(^{31}P$_1$) = [75, 35, 54] MHz; A(^{31}P$_2$) = [76, 64, 64] MHz; *A*(^{1}H) = ± [17.0, 22.0, 32.5] MHz; *A*(^{14}N) = [7.4, 7.4, 9] MHz.

[Fe(η^5-Cp*)(dppe)CO]BAr$^{F}_4$ ([**5**]BAr$^{F}_4$): This molecule and H$_2$ cleanly result (>99%) by annealing of solutions of *exo*- or *endo*-[**3**]$^+$ to room temperature. Characterization data is consistent with that reported in ref. 6.

[Fe(η^5-Cp*)(dppe)CNXyl]BAr$^{F}_4$ ([**6**]BAr$^{F}_4$): To a solution of **Fe^{II}(η^5-Cp*)(dppe)H** (9.5 mg, 0.016 mmol, 1 equiv.) and CNXyl (2.1 mg, 0.016 mmol, 1 equiv.) in Et$_2$O (2 mL) at -78 ˚C was added drop-wise a chilled (-78 ˚C) solution of [H(OEt)$_2$]BAr$^{F}_4$ (16.3 mg, 0.016 mmol, 1 equiv.) in Et$_2$O (1 mL). Following addition, the resulting mixture was stirred at 25 ˚C over 10 min giving a clear yellow solution. Removal of volatiles *in-vacuo* and washing with pentane gave [**6**]BAr$^{F}_4$ as a yellow solid (20 mg, 80%). **^{1}H NMR (THF-d$_8$, 400 MHz, 298 K)**: δ = 7.79 (s, 8H; BAr$^{F}_4$), 7.57 (s, 4H; BAr$^{F}_4$), 7.55 (m, 10H; Ph), 7.39 (m, 10H; Ph), 7.08 (t, $^3J_{H,H}$ = 7.2 Hz, 1H; CNXyl), 7.00 (d, $^3J_{H,H}$ = 7.2 Hz, 2H; CNXyl), 2.67 (m, 2H; CH$_2$), 2.45 (m, 2H; CH$_2$), 1.63 (s, 6H; CNXyl), 1.55 (s, 15H; Cp*). **^{31}P{^{1}H} NMR (THF-d$_8$, 162 MHz, 298 K)**: δ = 94.0. **^{13}C NMR (THF-d$_8$, 100 MHz, 298 K)**: δ = 162.5 (q, $^1J_{C,B}$ = 37 Hz, BAr$^{F}_4$, ipso quaternary C), 135.6 (BAr$^{F}_4$, ortho C), 135.0, 134.6, 133.7, 131.9, 129.9, 129.9 (q, $^2J_{C,F}$ = 31 Hz, BAr$^{F}_4$, meta quaternary C), 129.6, 129.4, 129.2, 129.1, 125.4 (q, $^1J_{C,F}$ = 273 Hz, BAr$^{F}_4$, CF$_3$), 117.9 (m, BAr$^{F}_4$, para C), 93.6 (Cp*), 30.5 (CH$_2$; dppe), 18.8, 10.1 (Cp*). **IR (THF film)**: 2050 cm^{-1} ($\upsilon_{C\equiv N}$). **^{57}Fe Mössbauer (80 K, Et$_2$O solution, mm/s)**: δ = 0.16, ΔE_Q = 1.75.

[Fe(η^5-Cp*)(dppe)N$_2$]BAr$^{F}_4$ ([**7**]BAr$^{F}_4$): To a solution of Fe(η^5-Cp*)(dppe)CH$_3$[1] (21.8 mg, 0.036 mmol, 1 equiv.) in Et$_2$O (2 mL) at -78 ˚C was added drop-wise a chilled (-78 ˚C) solution of [H(OEt)$_2$]BAr$^{F}_4$ (36.5 mg, 0.036 mmol, 1 equiv.) in Et$_2$O (1 mL). Following addition, the resulting mixture was stirred at 25 ˚C over 10 min giving a clear yellow solution. Removal of volatiles *in-vacuo* and washing with pentane gave [**7**]BAr$^{F}_4$ as a yellow solid (53 mg, 92%). [**7**]BAr$^{F}_4$ is also the product of H$_2$ release by [**1**]BAr$^{F}_4$ in THF (< 5% yield after 1 week, + 80 ^{o}C, THF-d$_8$). **^{1}H NMR (THF-d$_8$, 400 MHz, 298 K)**: δ = 7.79 (s, 8H; BAr$^{F}_4$), 7.57 (s, 4H; BAr$^{F}_4$), 7.75-7.54 (m, 16H; Ph), 7.44 (m, 4H; Ph), 2.54 (m, 2H; CH$_2$), 2.38 (m, 2H; CH$_2$), 1.43 (s, 15H; Cp*). **^{31}P{^{1}H} NMR (THF-d$_8$, 162 MHz, 298 K)**: δ = 86.6. **^{13}C NMR (THF-d$_8$, 100 MHz, 298 K)**: δ = 162.5 (q, $^1J_{C,B}$ = 37 Hz, BAr$^{F}_4$, ipso quaternary C), 135.6 (BAr$^{F}_4$, ortho C), 135.4, 134.3, 133.2, 132.4, 132.2, 129.9 (q, $^2J_{C,F}$ = 31 Hz, BAr$^{F}_4$, meta quaternary C), 125.4 (q, $^1J_{C,F}$ = 273 Hz, BAr$^{F}_4$, CF$_3$), 118.0 (m, BAr$^{F}_4$, para C), 117.0, 92.7 (Cp*), 28.8 (CH$_2$; dppe), 9.2 (Cp*). **IR (THF film)**: 2119 cm^{-1} (υ_{NN}).

3. Spectroscopic Data

Figure S2. [**1**]BAr^F_4, ^1H NMR, THF-d_8, 400 MHz, 298 K

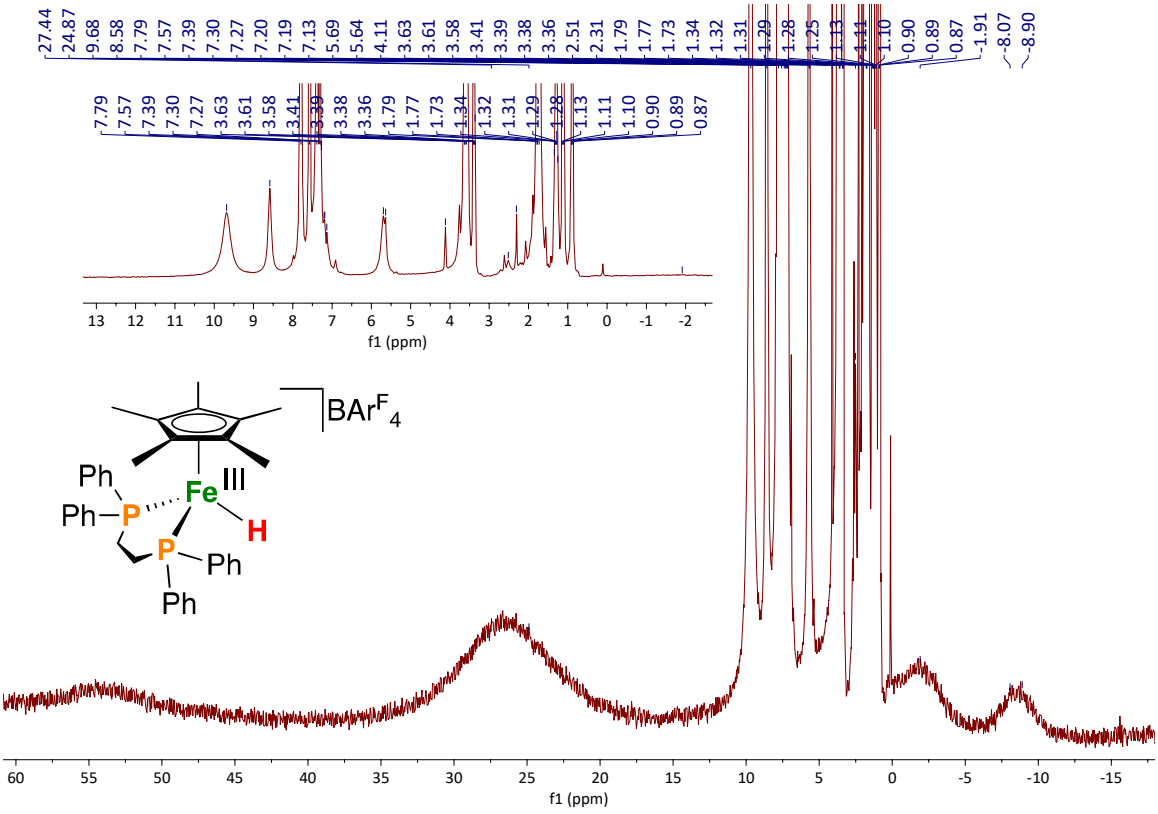

Note: The $^{31}P\{^1H\}$ NMR spectrum (THF-d_8, 162 MHz, 298 K) is featureless.

Figure S3. [**1**]BAr^{F}_{4}, FT-IR ATR, thin film, 298 K (υ_{FeH} = 1874 cm^{-1})

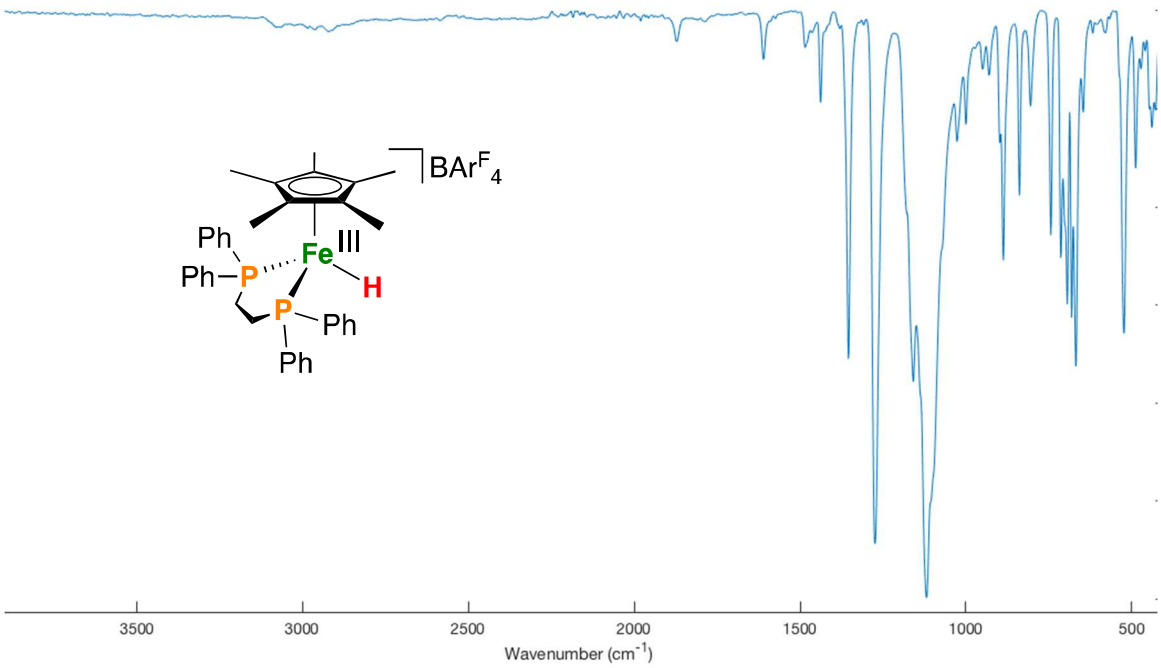

Figure S4. *endo*-**3**, ^{1}H NMR, C_6D_6, 400 MHz, 298 K. The data match that previously reported.[5] (* = C_6D_6)

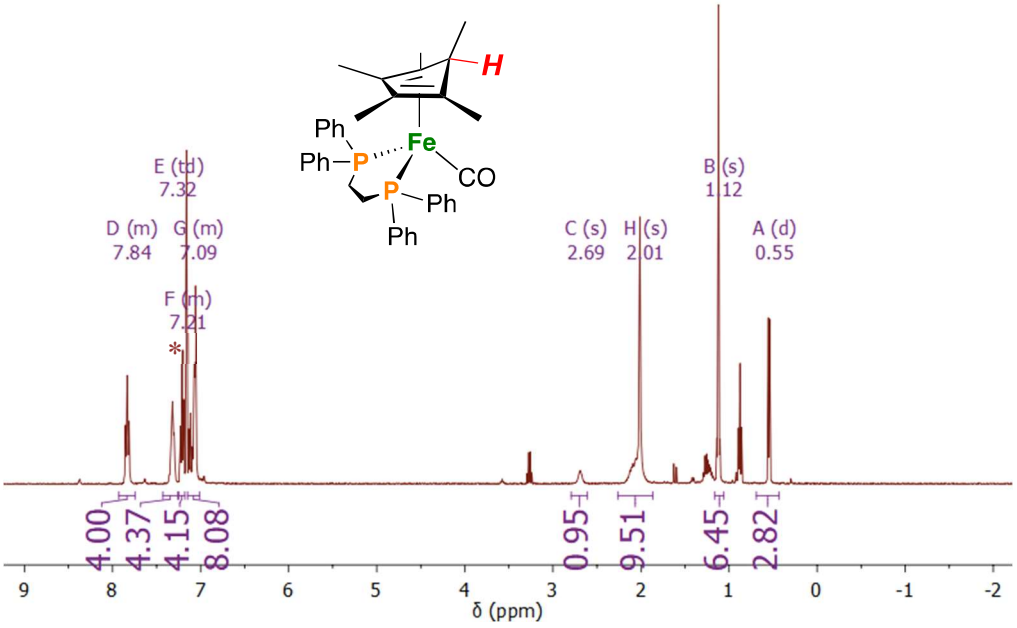

Figure S5. *endo*-**3-H/D** stacked plot, ^{1}H NMR, C_6D_6, 400 MHz, 298 K showing disappearance of a signal at $\delta_H = 2.65$.

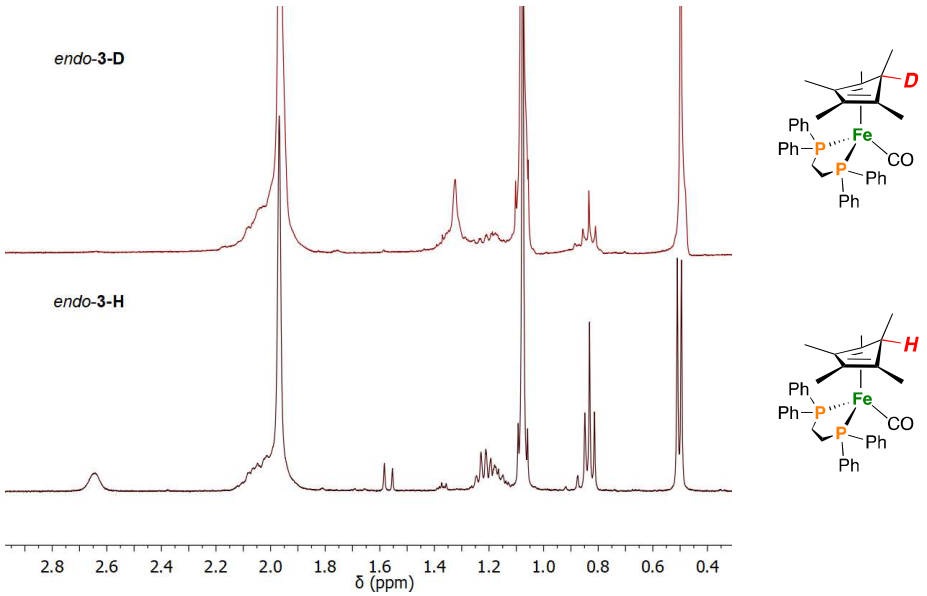

Figure S6 *endo*-**3**, $^{31}P\{^{1}H\}$ NMR, C_6D_6, 162 MHz, 298 K. The data match that previously reported.[5]

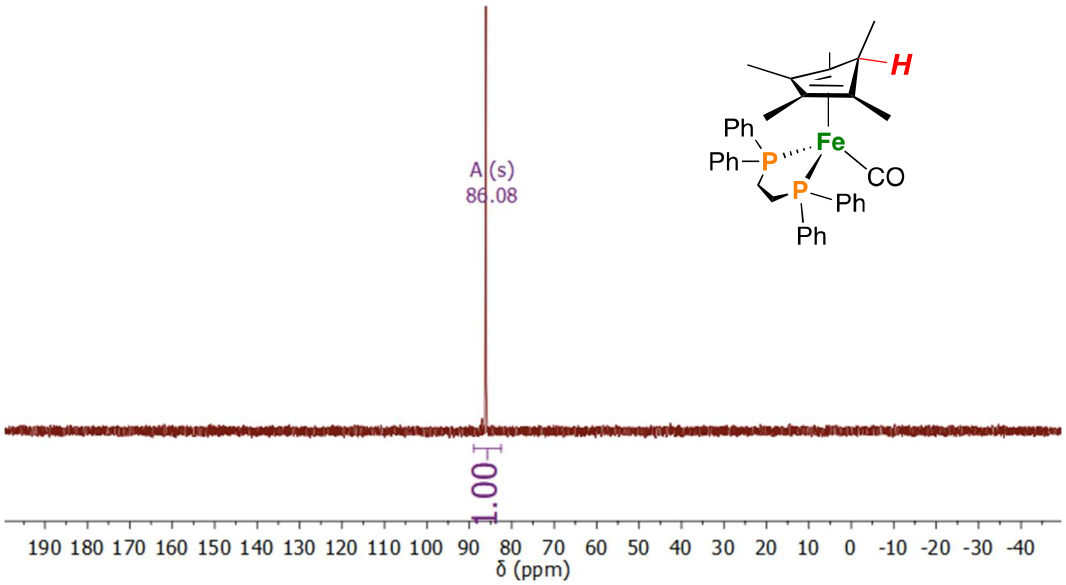

Figure S7. *endo*-**3-H/D**, FT-IR ATR, thin film, 298 K

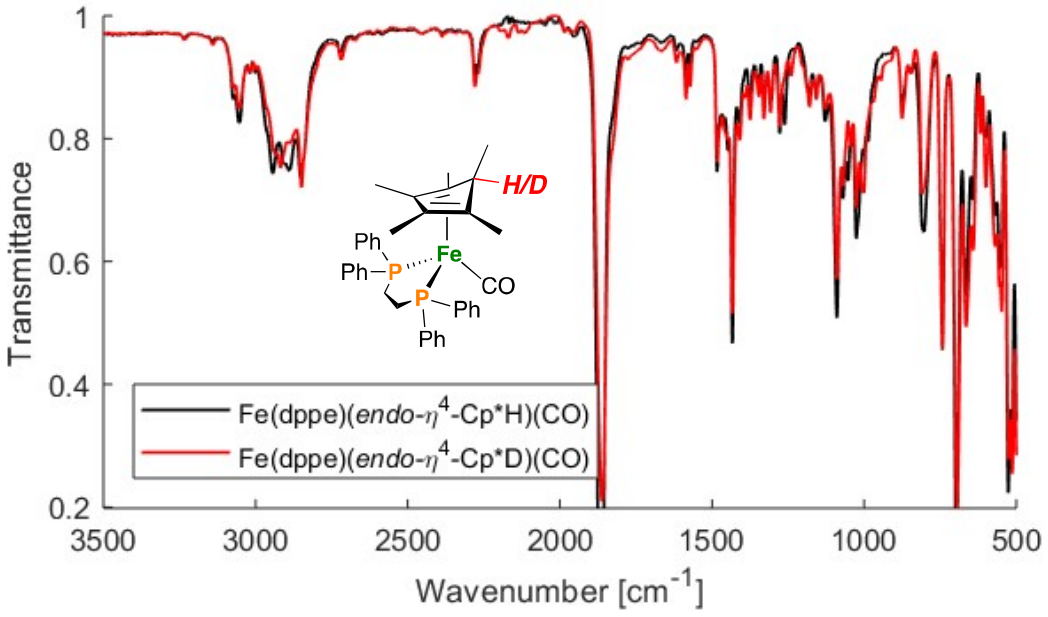

Figure S8. *exo*-**3**, ^{1}H NMR, C_6D_6, 400 MHz, 298 K (* = C_6D_6)

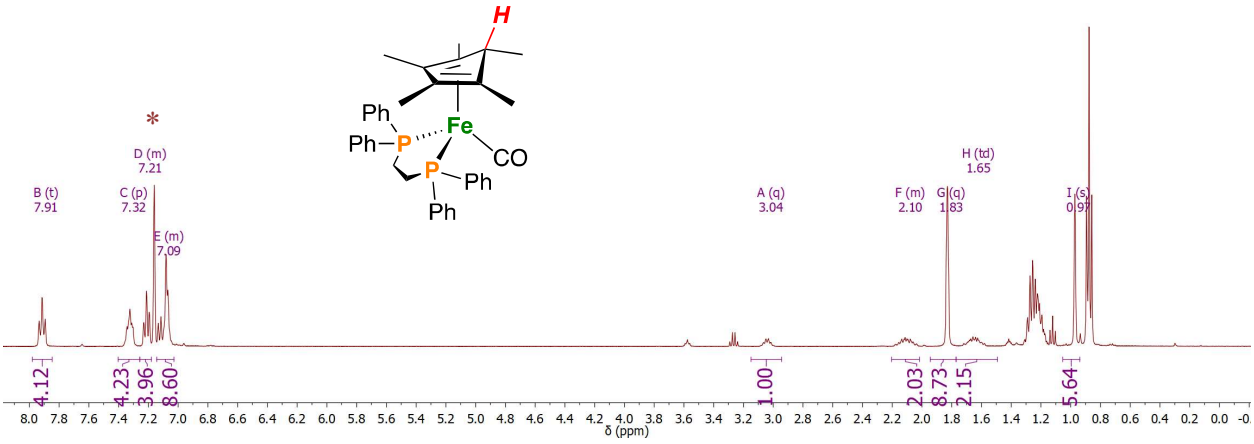

Figure S9. *exo*-**3-H/D** stacked plot, ^{1}H NMR, C_6D_6, 400 MHz, 298 K showing disappearance of a signal at $\delta_H = 2.65$.

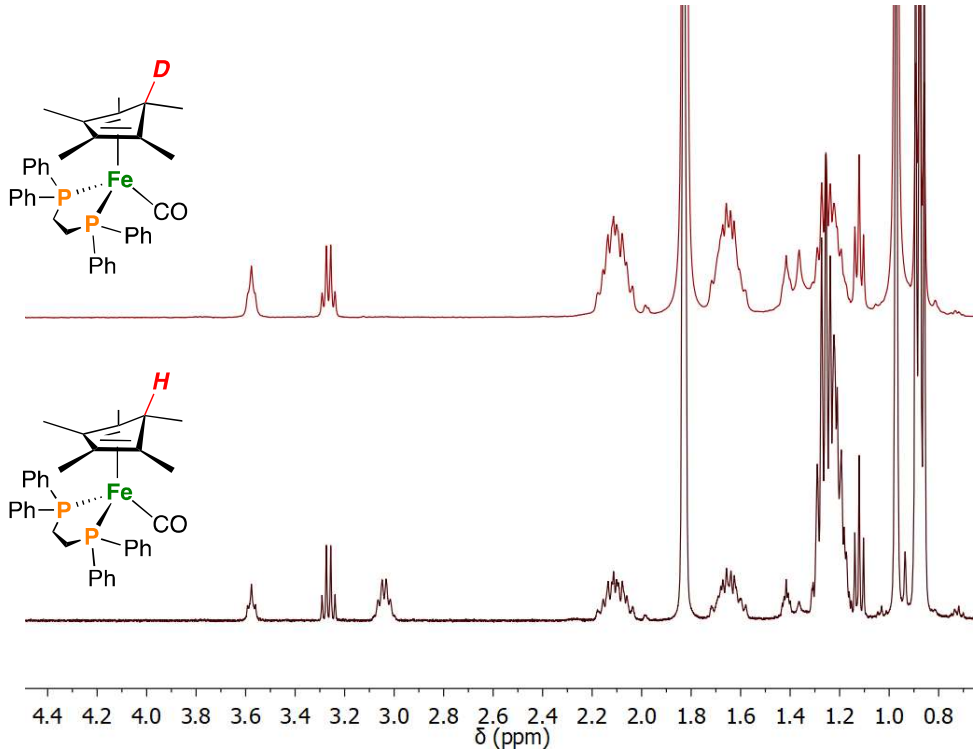

Figure S10. *exo*-**3**, $^{31}P\{^{1}H\}$ NMR, C_6D_6, 162 MHz, 298 K

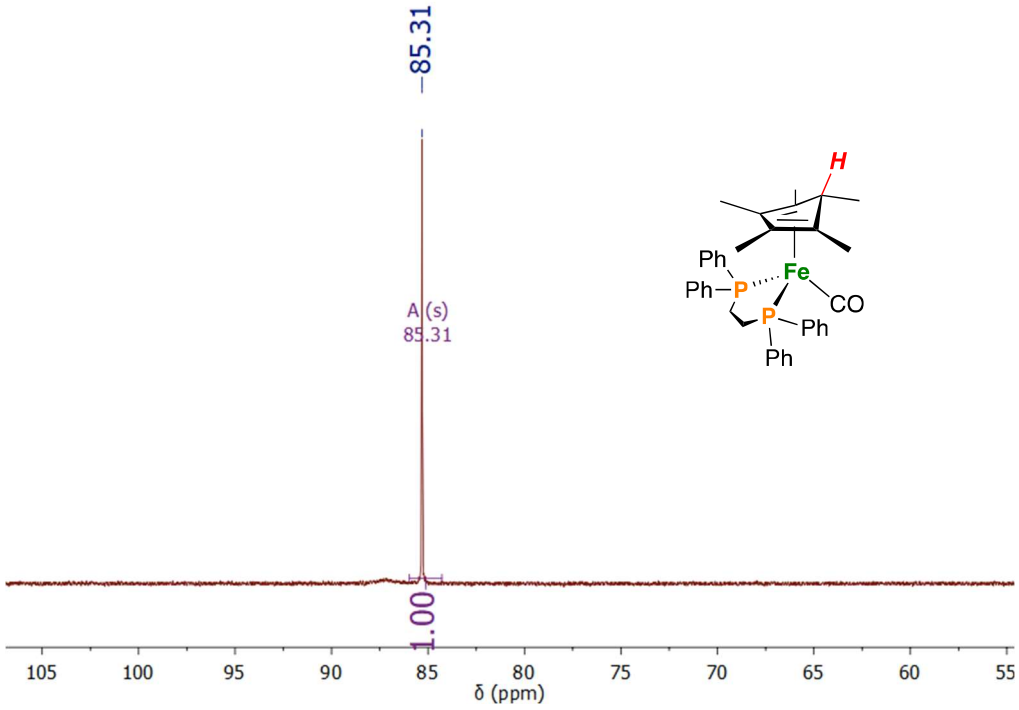

Figure S11. *exo*-**3**, $^{13}C\{^{1}H\}$ NMR, THF-d_8, 100 MHz, 298 K (* = THF-d_8)

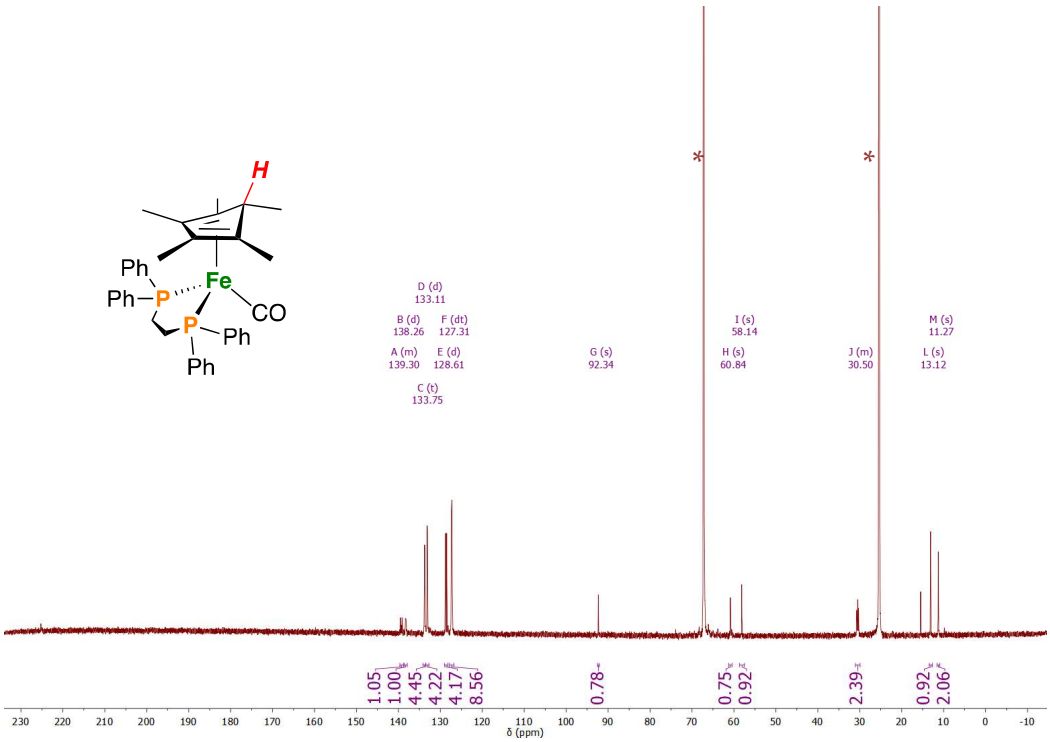

Figure S12. *exo*-**3-H/D**, FT-IR ATR, thin film, 298 K (*exo*-**3-H**: 2711 and 2612 cm^{-1} and *exo*-**3-D:** 2009 and 1955 cm^{-1}).

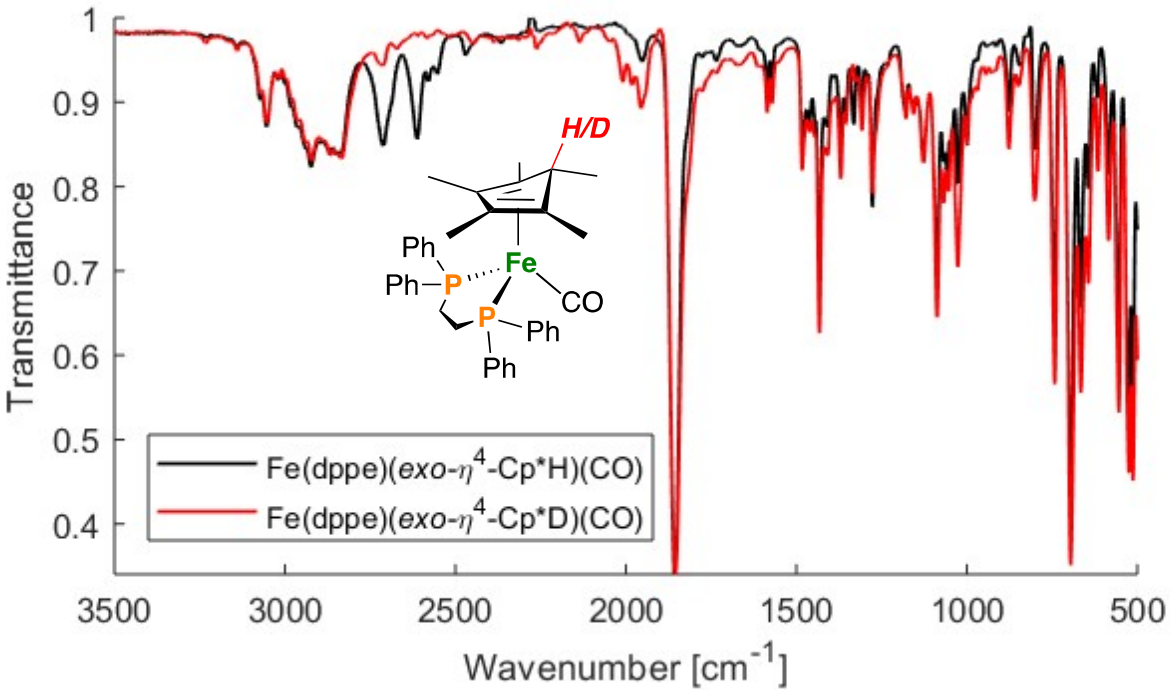

Figure S13. [**5**]BAr^{F}_{4}, ^{1}H NMR, THF-d_8, 400 MHz, 298 K (this compound is formed from H_2 evolution from 0.5 equiv. *exo-*/*endo*-[**3**]$^{+}$ - signals match those previously provided in ref. 6). (* = THF-d_8)

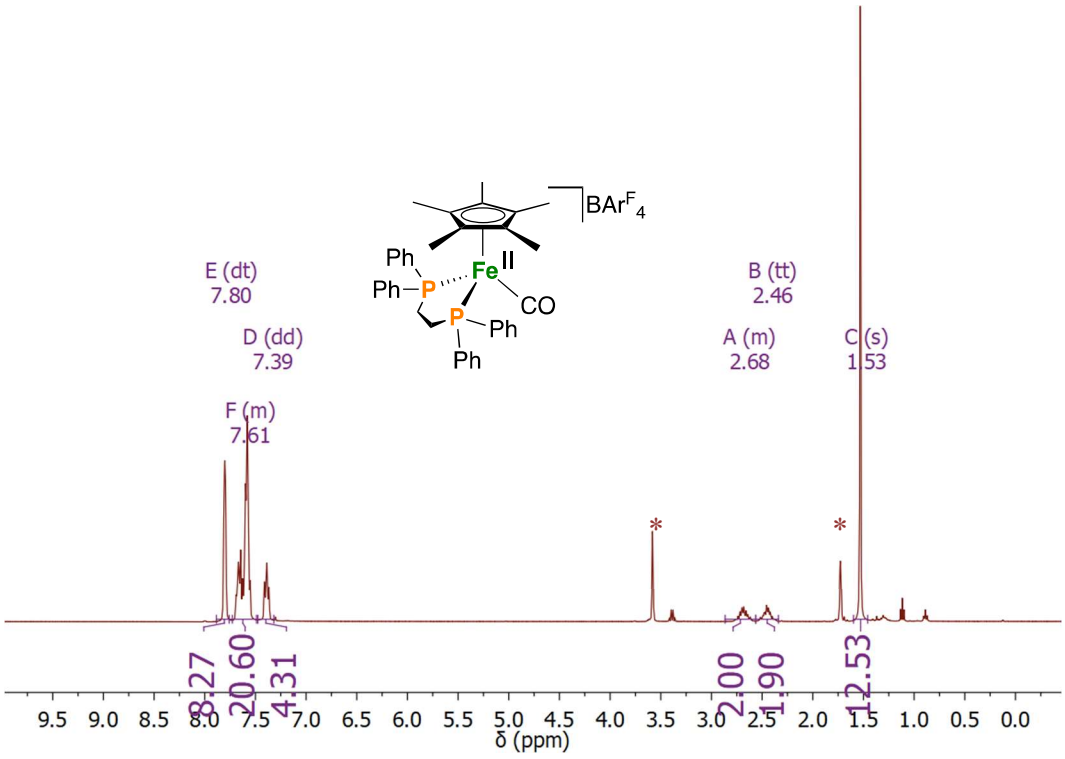

Figure S14. [**5**]BAr^F_4, $^{31}P\{^1H\}$ NMR, THF-d_8, 162 MHz, 298 K ((this compound is formed from H_2 evolution from 0.5 equiv. *exo*-/*endo*-[**3**]$^+$ - signals match those previously provided in ref. 6).

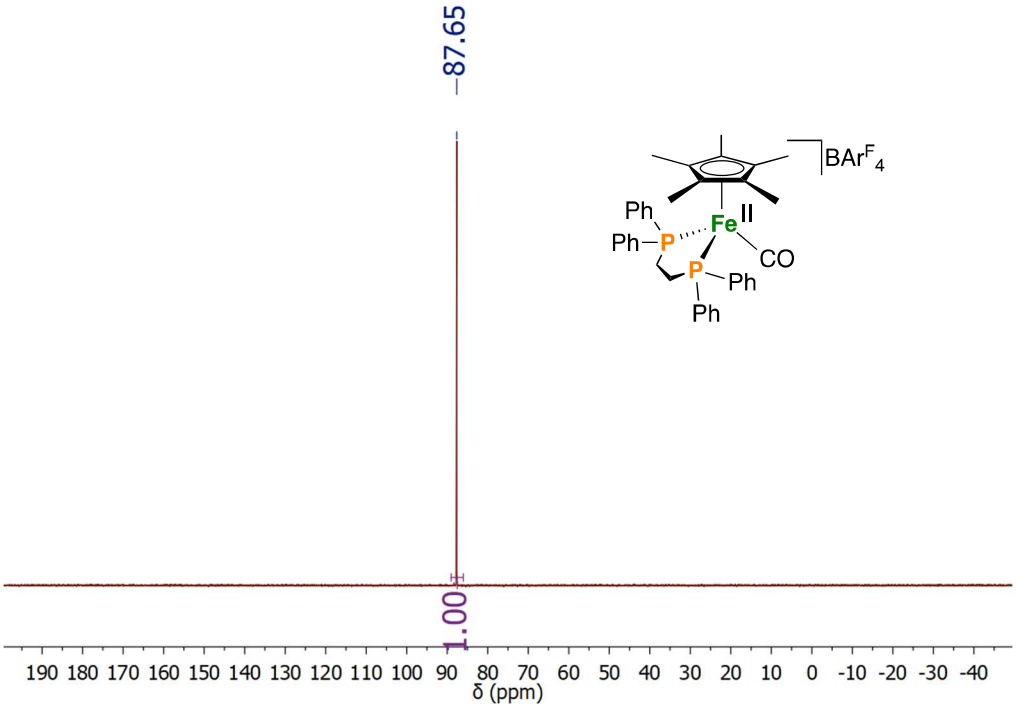

Figure S15. [**6**]BAr$^{F}_{4}$, ^{1}H NMR, THF-d$_8$, 400 MHz, 298 K (* = THF-d$_8$)

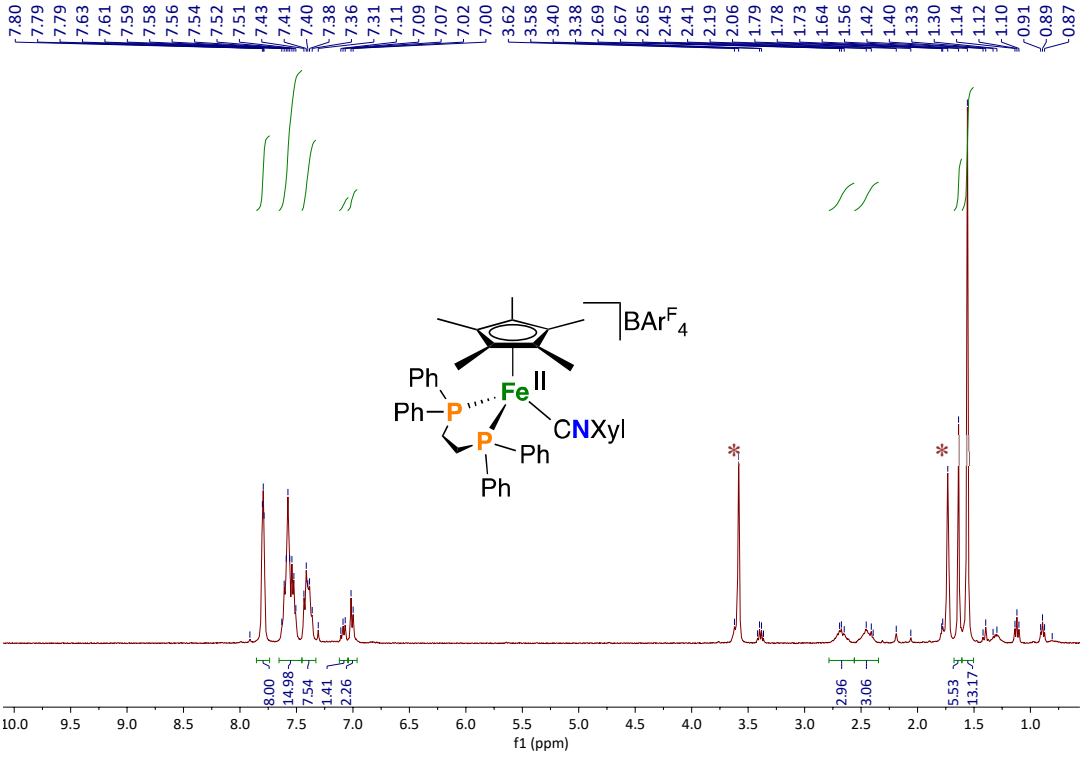

Figure S16. [**6**]BAr$^{F}_{4}$, ^{31}P{^{1}H} NMR, THF-d$_8$, 162 MHz, 298 K

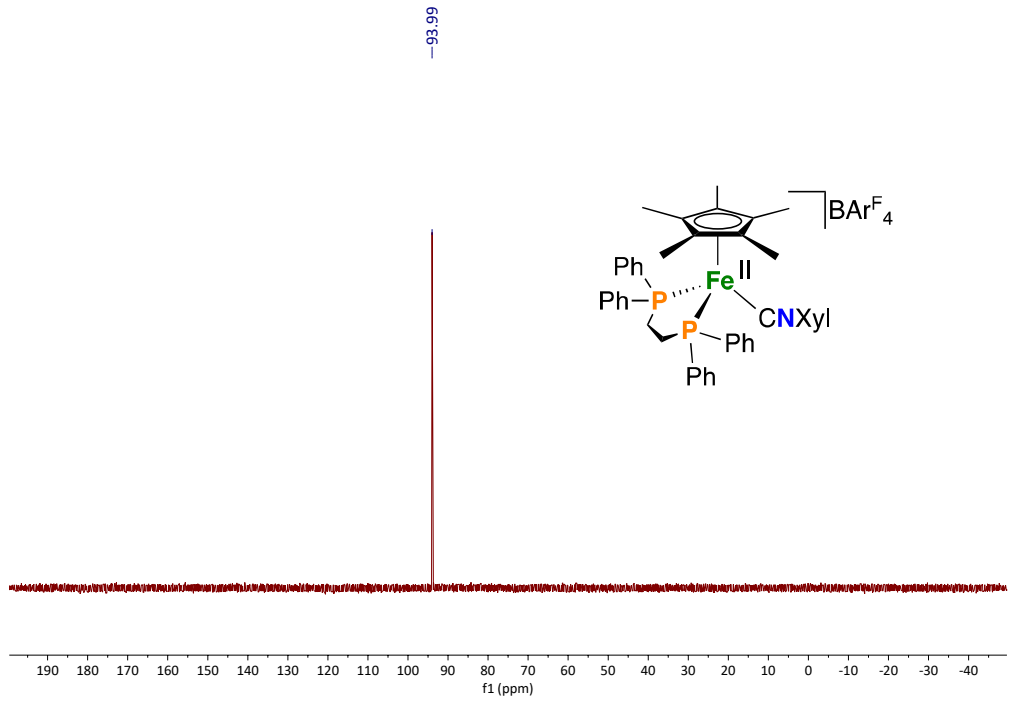

Figure S17. [**6**]BAr^{F}_{4}, $^{13}C\{^{1}H\}$ NMR, THF-d_8, 100 MHz, 298 K (* = THF-d_8)

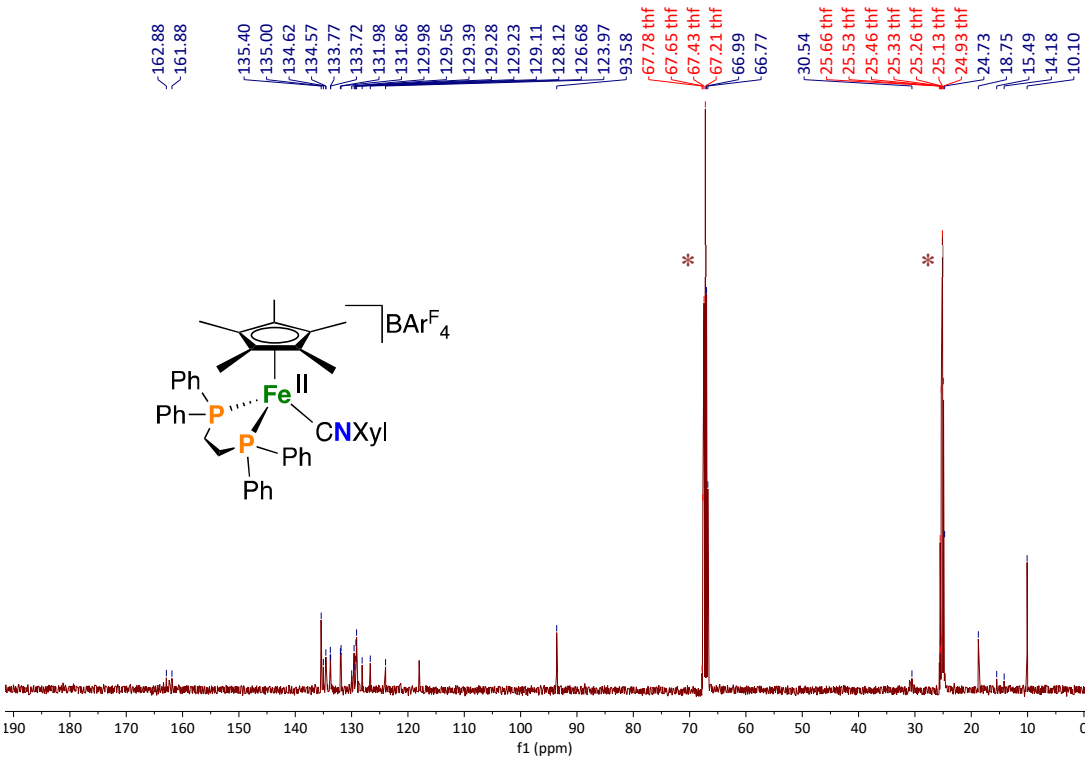

Figure S18. [**6**]BAr^{F}_{4}, FT-IR ATR, thin film, 298 K (υ_{CN} = 2050 cm^{-1})

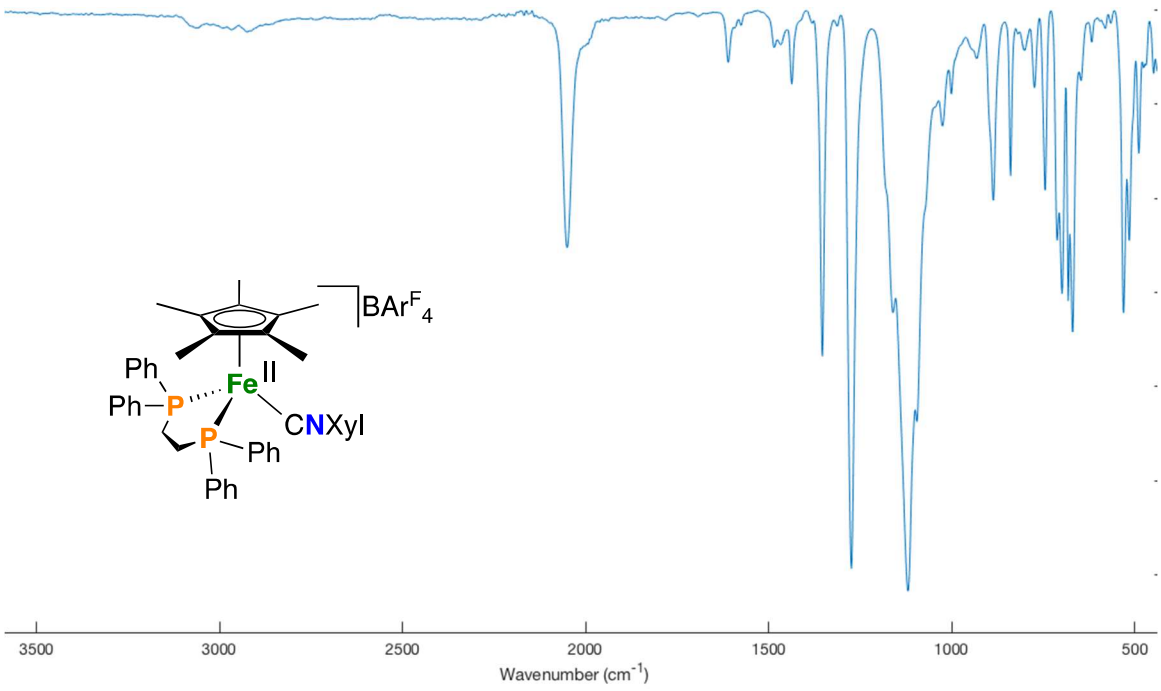

Figure S19. CNXyl, FT-IR ATR, thin film, 298 K (υ_{CN} = 2151 cm^{-1})

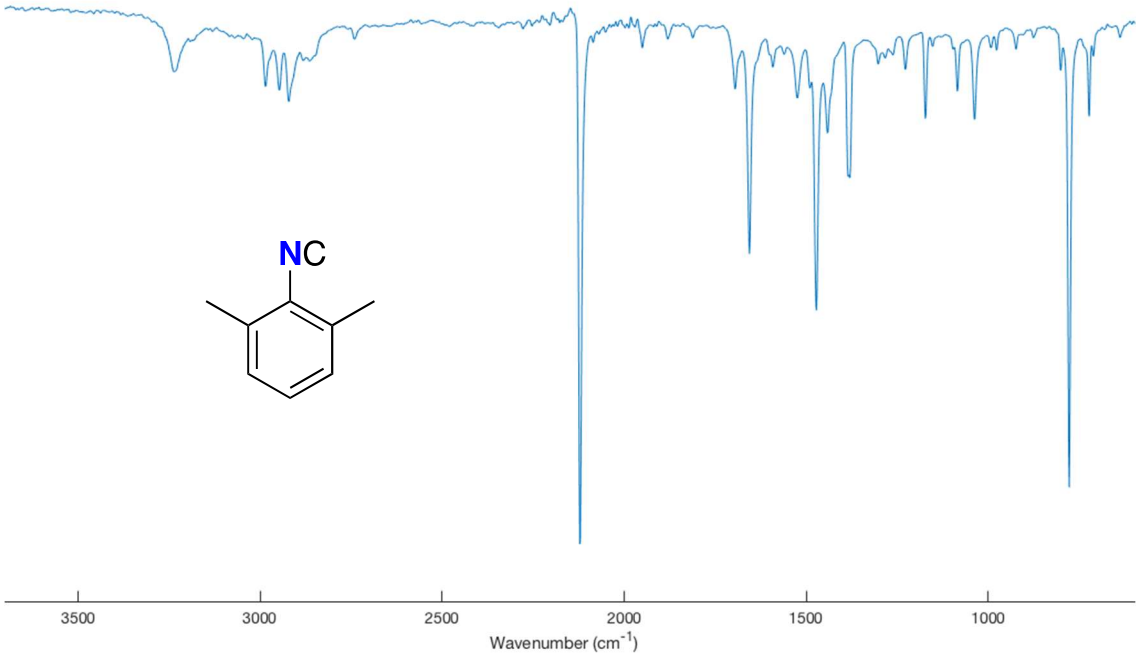

3.1 H_2 Evolution by [1]BAr^F_4 in THF:

To a J-Young NMR tube containing THF-d_8 (606 mg) was added [**1**]BAr^F_4 (4.9 mg, 0.003 mmol). The reaction mixture was monitored by NMR spectroscopy, showing no observable reaction. However, heating the reaction mixture at 80 °C for 24 h results in minimal (<5 % deterioration) to give [Fe^{II}(η^5-Cp*)(dppe)(N_2)]BAr^F_4 ([**7**]BAr^F_4) and H_2. [**2**]BAr^F_4 is cleanly accessible on preparative scale by protonation of Fe^{II}(η^5-Cp*)(dppe)CH_3 using [H(OEt_2)]BAr^F_4 (*as outlined above*).

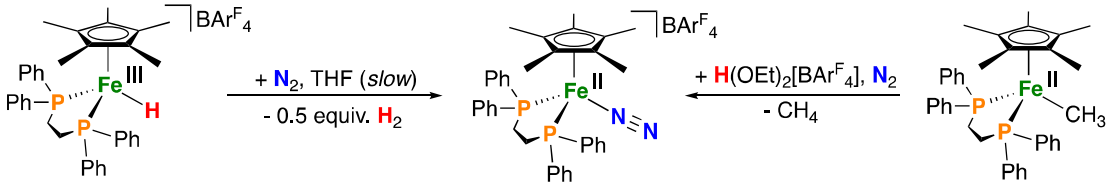

Figure S20. Heating [**1**]BAr^F_4 at 80 °C, ^{1}H NMR, THF-d_8, 400 MHz, 298 K (**Red**; 1 h, **green**; 5 h, **blue**; 23 h); dppe(CH_2) and Cp*(CH_3) groups for [**7**]BAr^F_4 highlighted in pink.

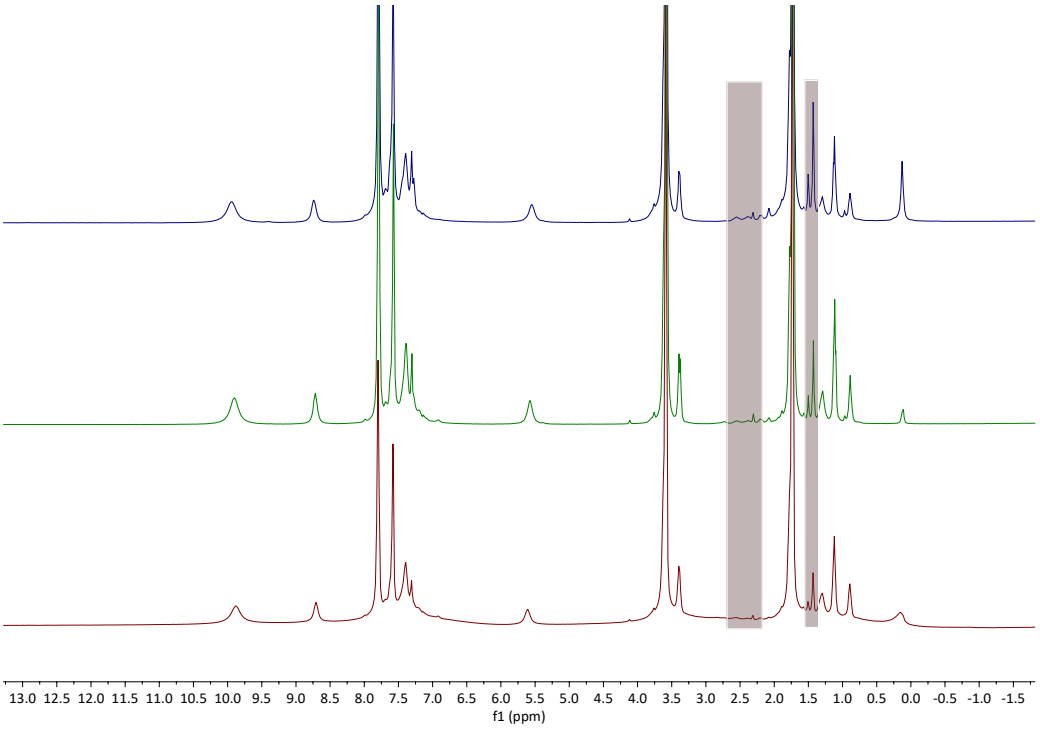

Figure S21. Heating [**1**]BAr^{F}_{4} at 80 °C, $^{31}P\{^{1}H\}$ NMR, THF-d_8, 162 MHz, 298 K (**Red**; 1 h, **green**; 5 h, **blue**; 23 h) (free ligand at δ = -12.8 ppm).

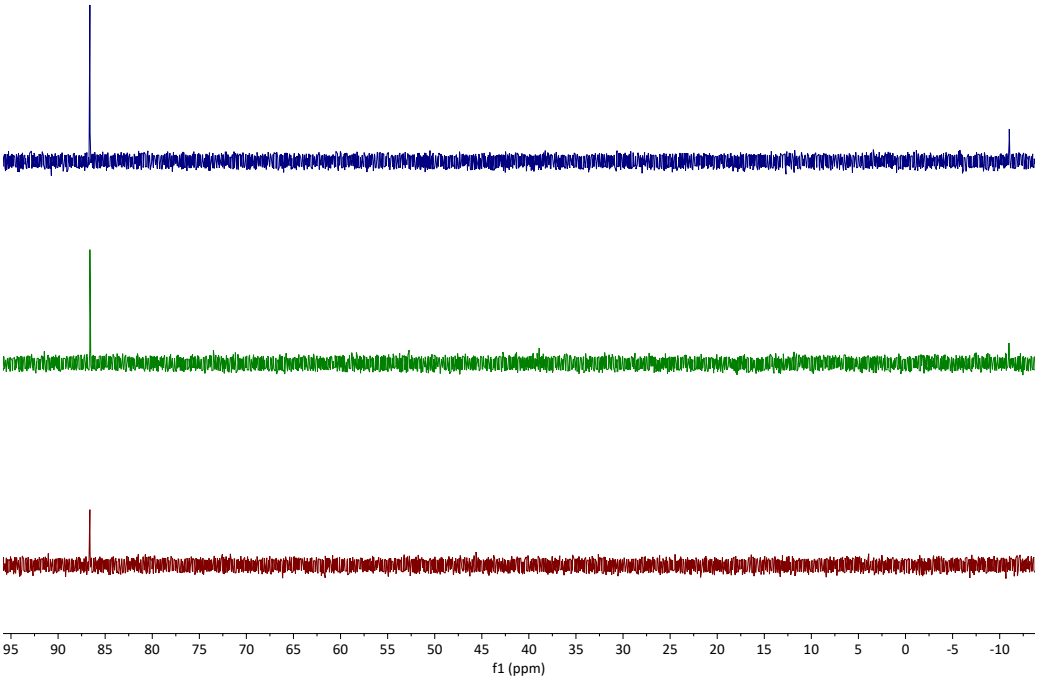

Figure S22. [**7**]BAr^{F}_{4}, ^{1}H NMR, THF-d_8, 400 MHz, 298 K (* = THF-d_8)

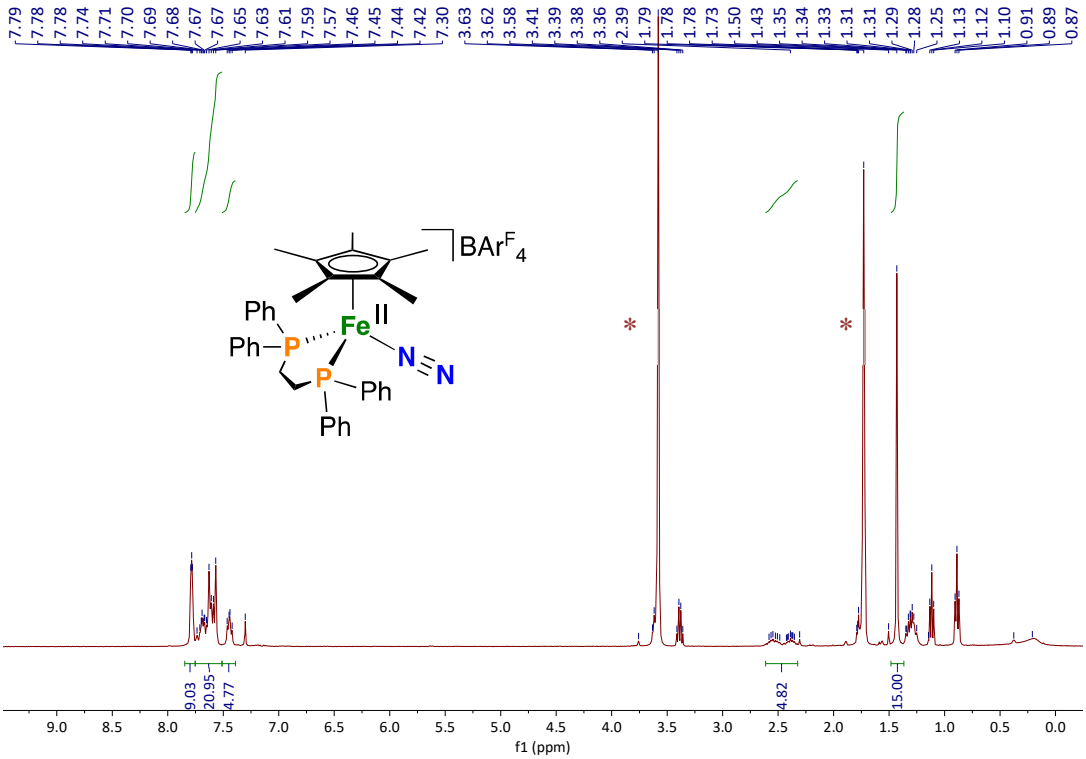

Figure S23. [**7**]BAr$^{F}_{4}$, ^{31}P{^{1}H} NMR, THF-d$_8$, 162 MHz, 298 K

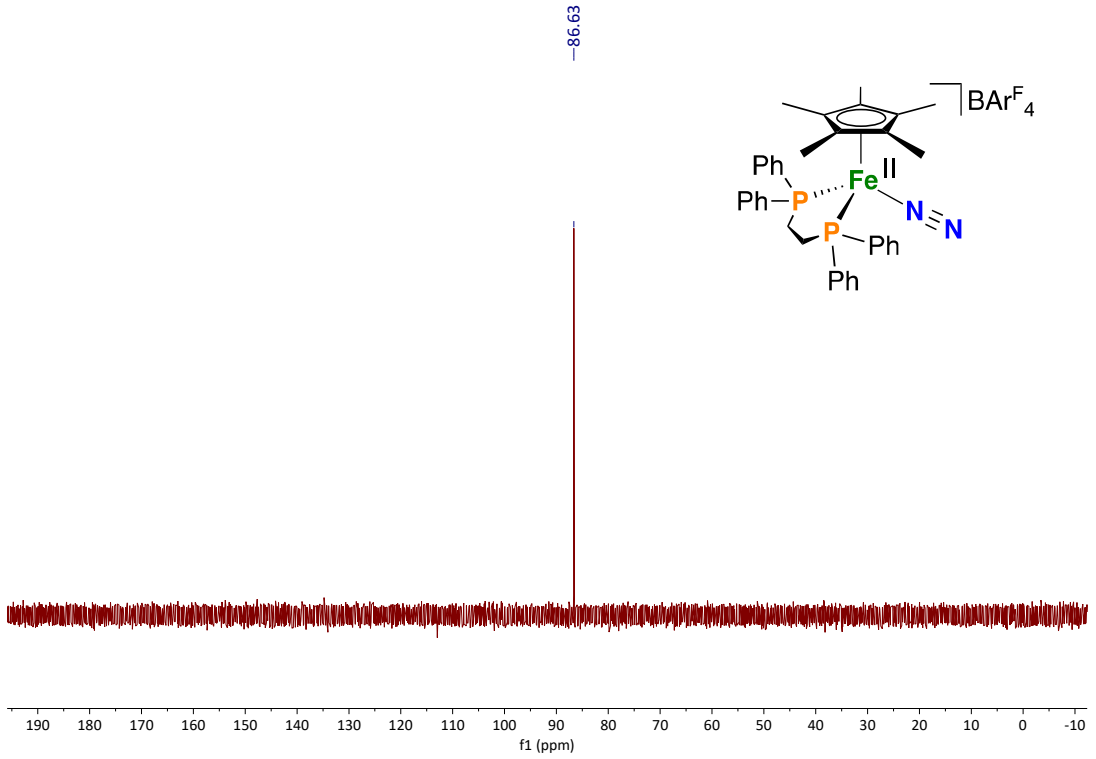

Figure S24. [**7**]BAr$^{F}_{4}$, ^{13}C{^{1}H} NMR, THF-d$_8$, 100 MHz, 298 K (* = THF-d$_8$)

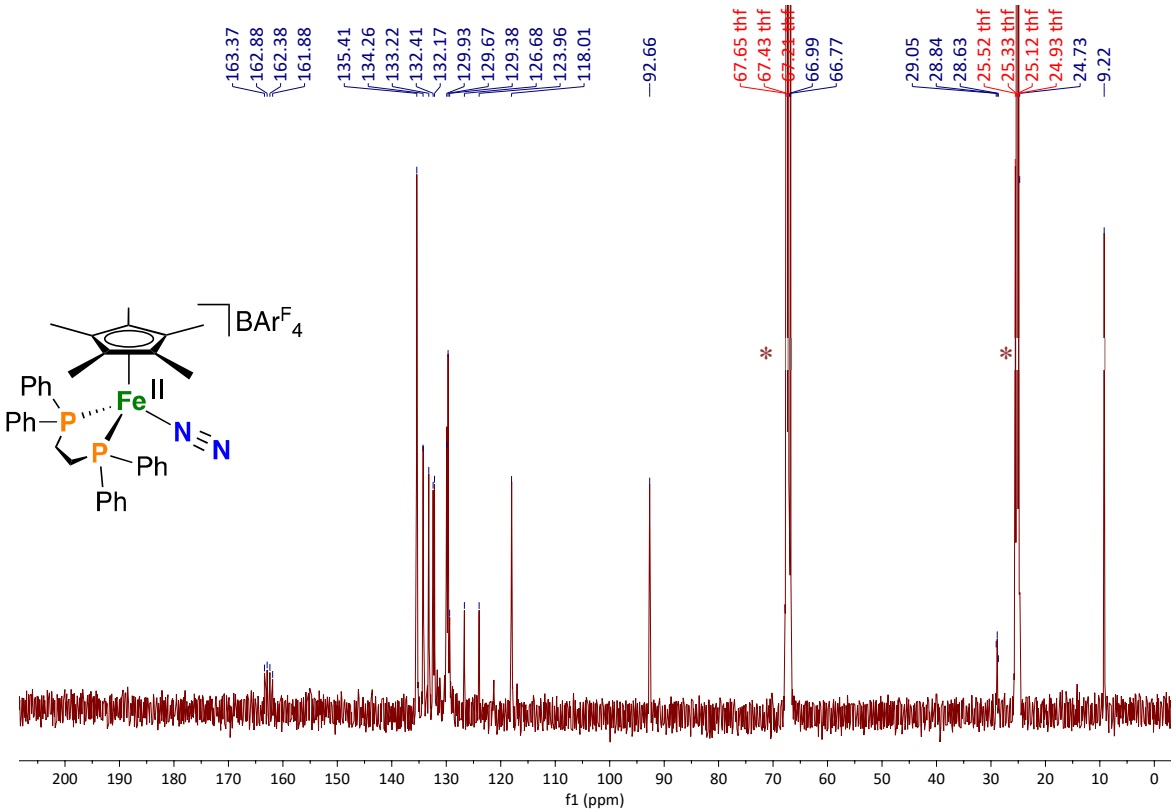

Figure S25. [**7**]BAr^{F}_{4}, FT-IR ATR, thin film, 298 K (υ_{NN} = 2119 cm^{-1})

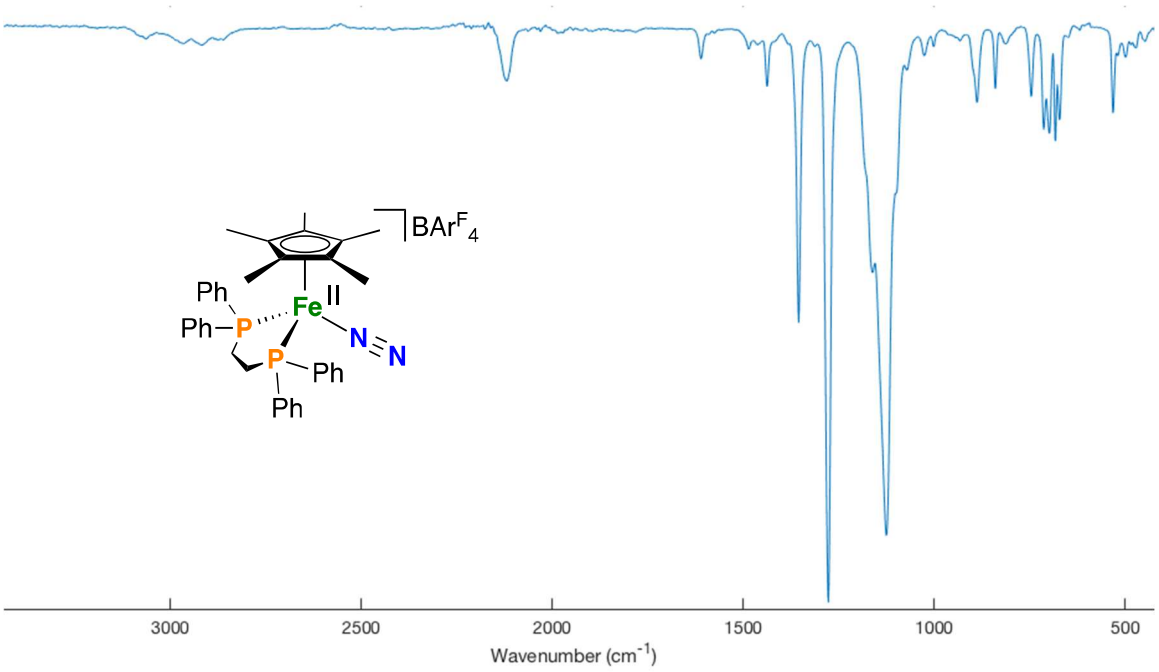

3.2 H_2 evolution by [1]BAr^F_4 in MeCN:

To a J-Young NMR tube containing MeCN-d_3 (646 mg) was added [**1**]BAr^F_4 (5.0 mg, 0.003 mmol). The reaction mixture was monitored by NMR spectroscopy, showing consumption of [**1**]BAr^F_4 to cleanly give [$Fe^{II}(\eta^5$-Cp*)(dppe)(NCMe)]BAr^F_4 ([**8**]BAr^F_4) and H_2.[7]

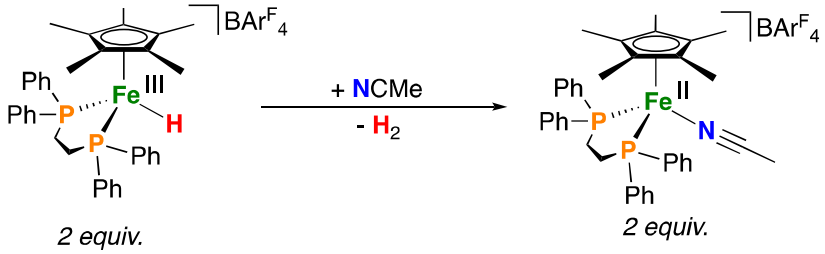

Figure S26. [**8**]BAr^F_4, ^{1}H NMR, ACN-d_3, 400 MHz, 298 K (inset shows signal for generated H_2 at δ = 4.57 ppm). (* = ACD-d_3)

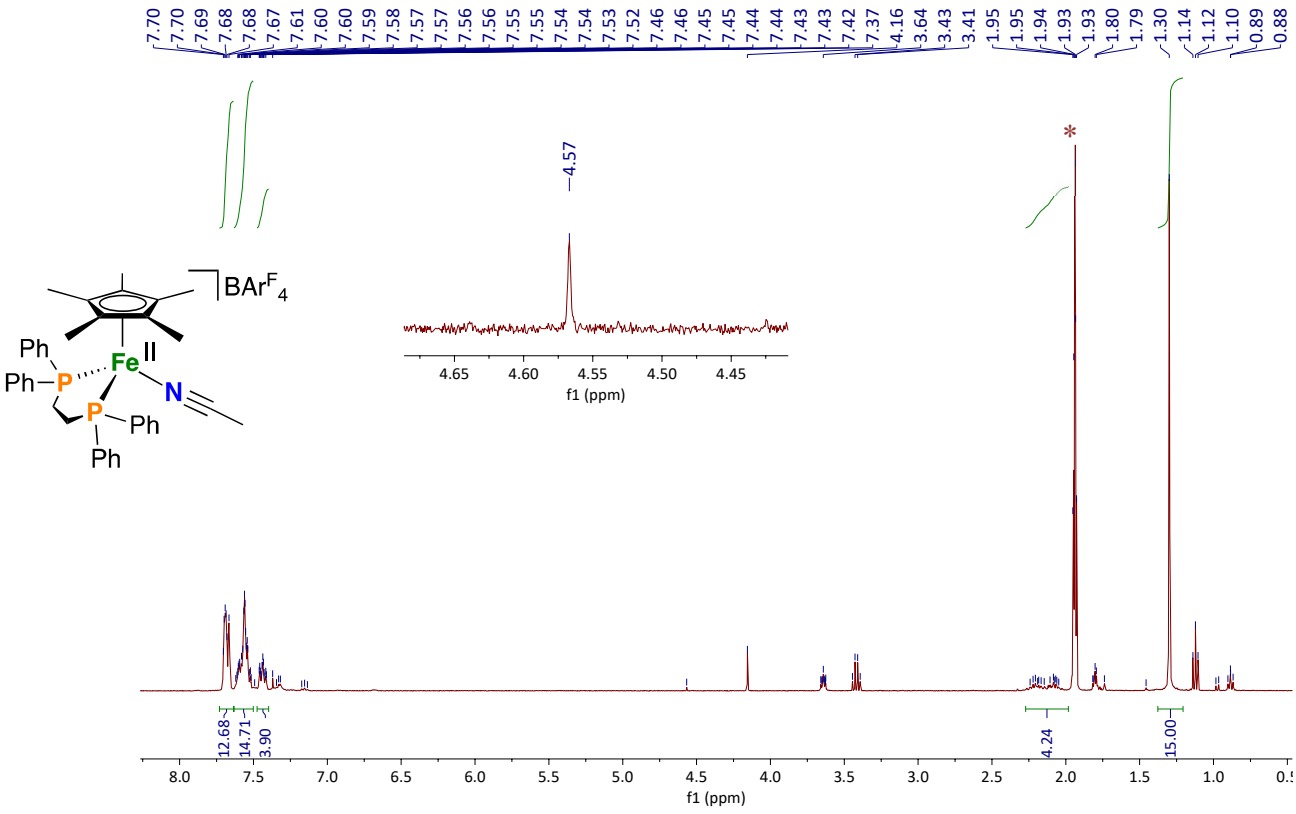

Figure S27. [**8**]BAr^{F}_{4}, $^{31}P\{^{1}H\}$ NMR, ACN-d_3, 162 MHz, 298 K

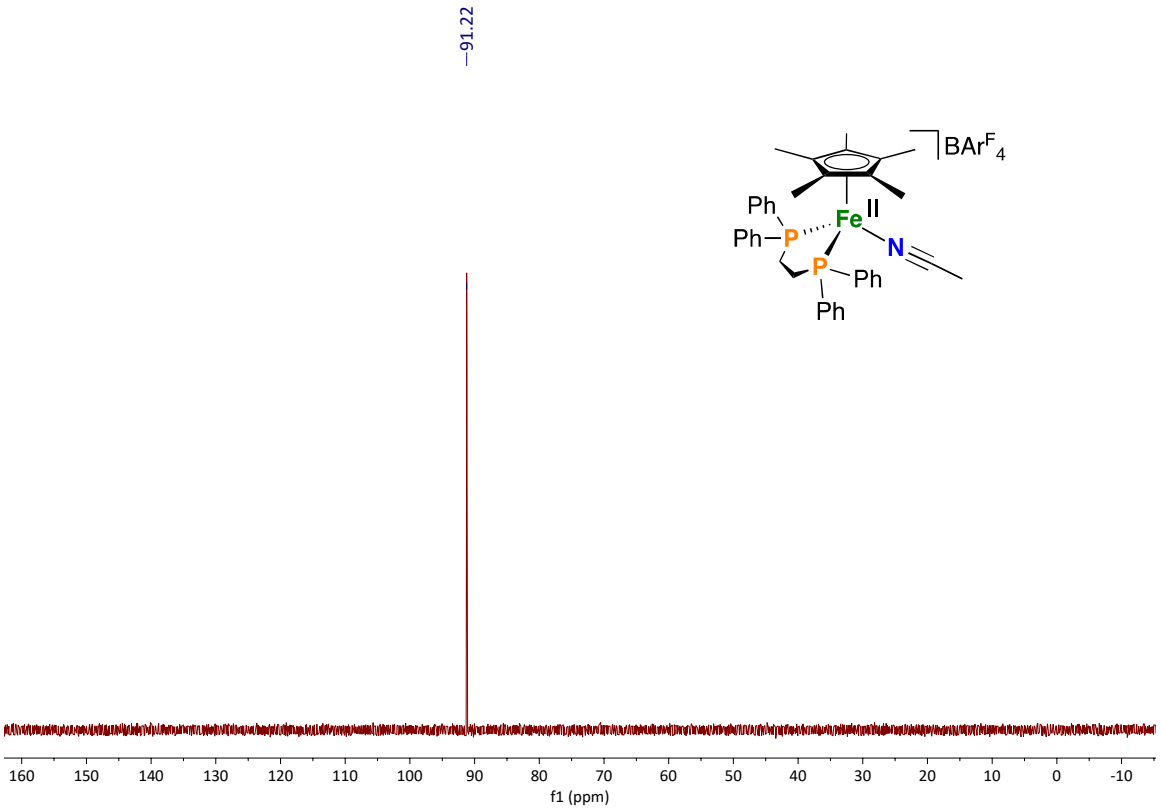

3.3 Hydricity measurement: Hydride transfer to CO_2:

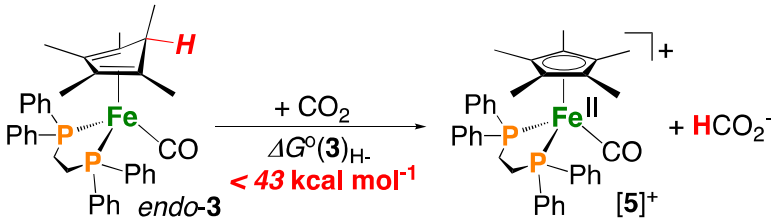

To an NMR J-Young tube containing a solution of *endo*-**3** (3.9 mg, 0.006 mmol, 1 equiv.) in d_3-acetonitrile (*ca.* 0.6 mL) was added CO_2. The reaction mixture was monitored by NMR spectroscopy, showing consumption of *endo*-**3** to give $[\mathbf{5}]^+$ and HCO_2^-.

Figure S28. $^{31}P\{^1H\}$ NMR, C_6D_6, 162 MHz, 298 K for the treatment of *endo*-**3** with CO_2 before addition, 5 days, 1 week, and 3 weeks post addition showing consumption of *endo*-**3** (δ_P = 84.5 ppm) and formation of $[\mathbf{5}]^+$ (δ_P = 89.8 ppm).

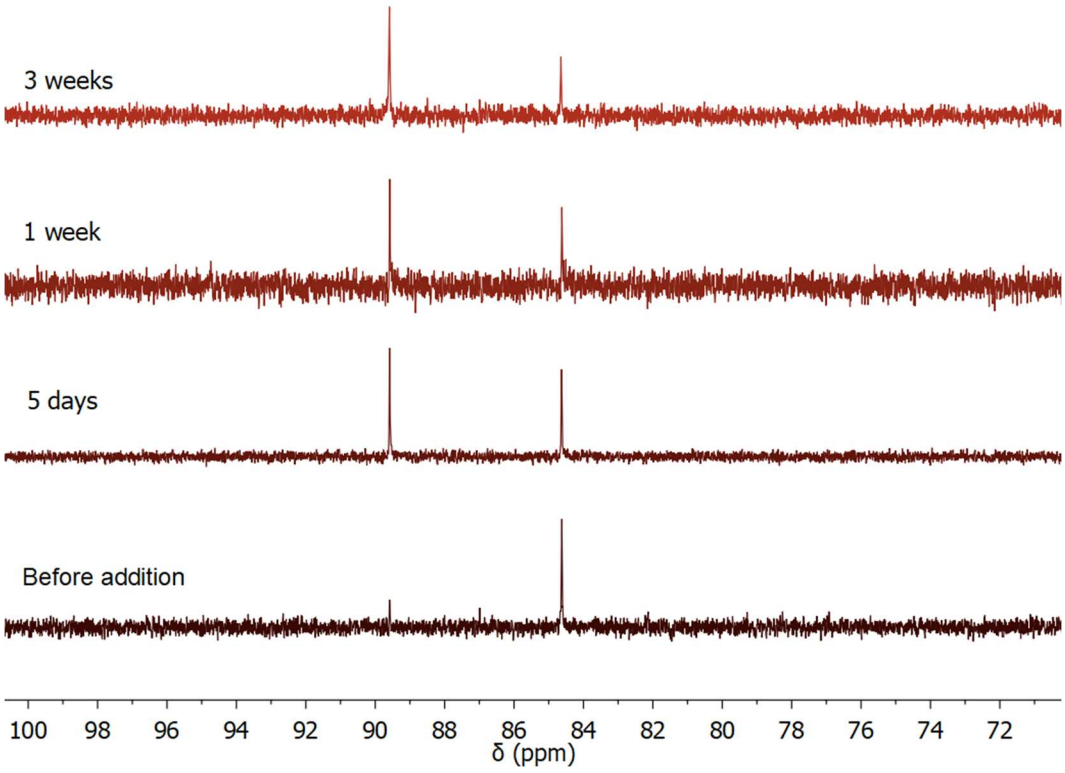

Figure S29. ^{1}H NMR, C_6D_6, 162 MHz, 298 K for the treatment of *endo*-**3** with CO_2 before addition, 5 days, 1 week, and 3 weeks post addition showing formation of HCO_2^- at δ_H = 8.6 ppm)

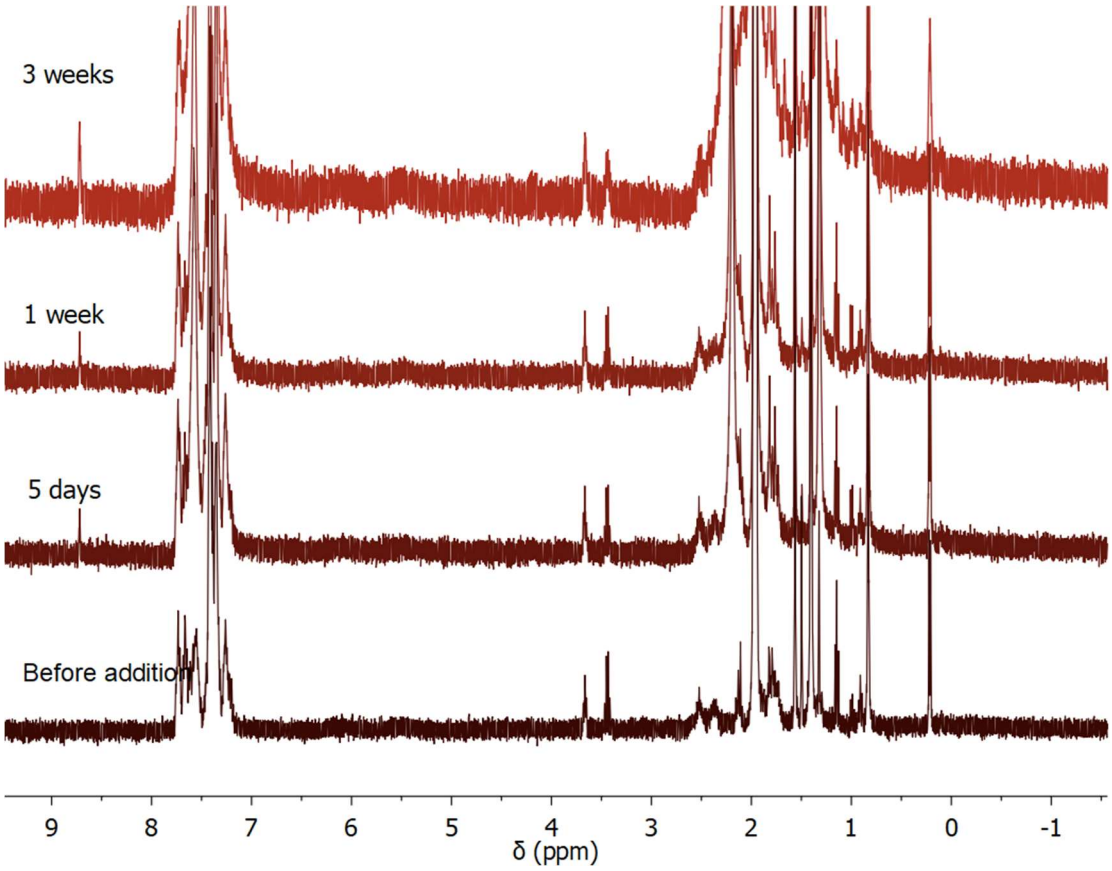

3.4 Azobenzene reduction:

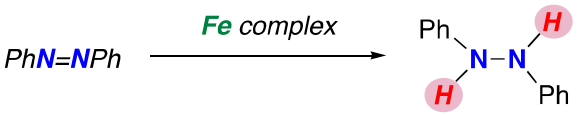

Using [**1**]$^+$: To a J-Young NMR tube containing a solution of [**1**]$^+$ (14.5 mg, 1 mmol) in d_8-THF (*ca.* 500 µL) was added PhNNPh (36 mg, 20 mmol). The reaction mixture was monitored by NMR spectroscopy, showing no reaction.

Azobenzene reduction by addition of CO: On top of a 0.5 mL of a frozen diethyl ether solution containing 2 µmol azobenzene and 0.1 µmol of *endo*/*exo*-[**3**]$^+$ was layered 0.25 mL of a 0.4 mM FcBArF solution in diethyl ether. The reaction mixture was stirred at −78 °C for 30 minutes followed by 10 minutes at room temperature. The solvent was removed *in vacuo* and the residue was dissolved in 0.6 mL C_6D_6 with trimethylbenzene as internal standard and analyzed by NMR.

General procedure for azobenzene reduction by oxidation: On top of a 0.5 mL of a frozen diethyl ether solution containing 2 µmol azobenzene and 0.1 µmol of *endo*/*exo*-[**3**]$^+$ was layered 0.25 mL of a 0.4 mM FcBArF solution in diethyl ether. The reaction mixture was stirred at −78 °C for 30 minutes followed by 10 minutes at room temperature. The solvent was removed *in vacuo* and the residue was dissolved in 0.6 mL C_6D_6 with trimethylbenzene as internal standard and analyzed by NMR.

Table S1. Summary of azobenzene reduction yields based on transferred H-atom equivalents

Fe complex	**Yield**
[**1**]$^+$	no reaction
endo-[**3**]$^+$	25 %
exo-[**3**]$^+$	78 %

Figure S30. ^{1}H NMR, C_6D_6, 400 MHz, 298 K showing the aromatic region following treatment of *endo*-[**3**]$^{+}$ with azobenzene to give [**5**]$^{+}$ and PhNHNHPh. **Bottom trace**: PhNNPh; **Middle trace**: oxidation of *endo*-**3** using [Fc]BAr^{F}_{4} to give *endo*-[**3**]$^{+}$ in the presence of azobenzene, giving PhNHNHPh, and **Top trace**, the reaction mixture spiked with authentic PhNHNHPh.

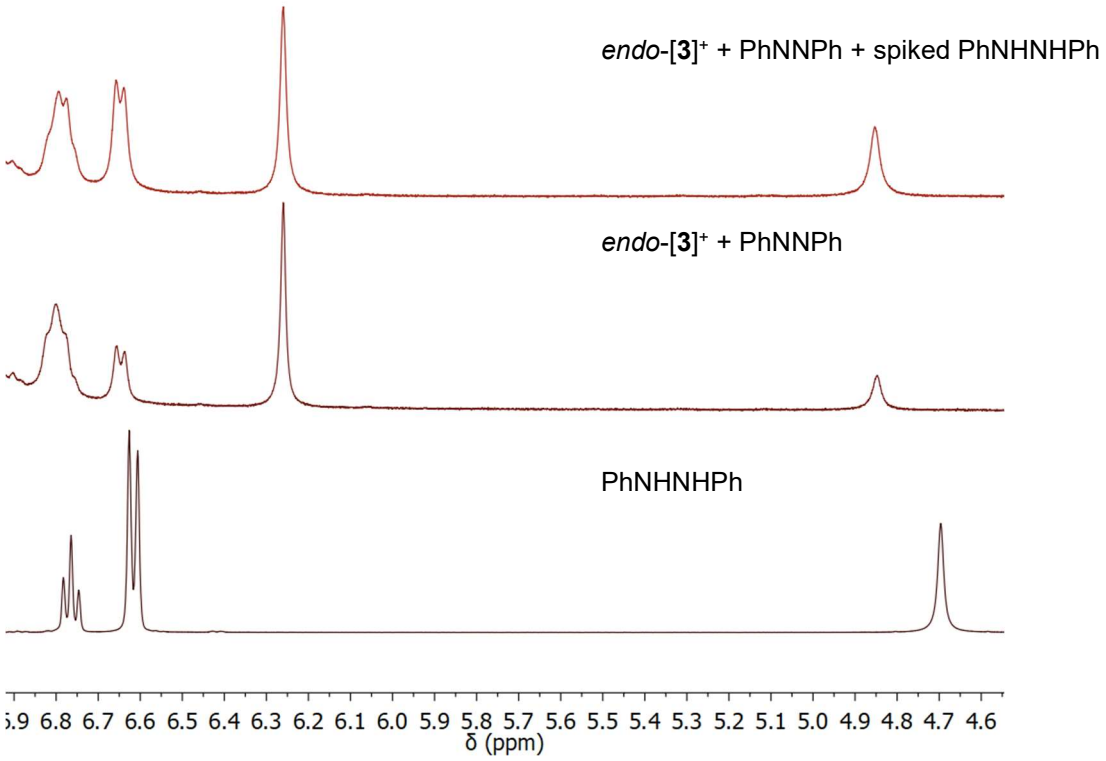

Figure S31. $^{31}P\{^{1}H\}$ NMR, C_6D_6, 162 MHz, 298 K following treatment of *endo*-[**3**]$^+$ with azobenzene to give [**5**]$^+$.

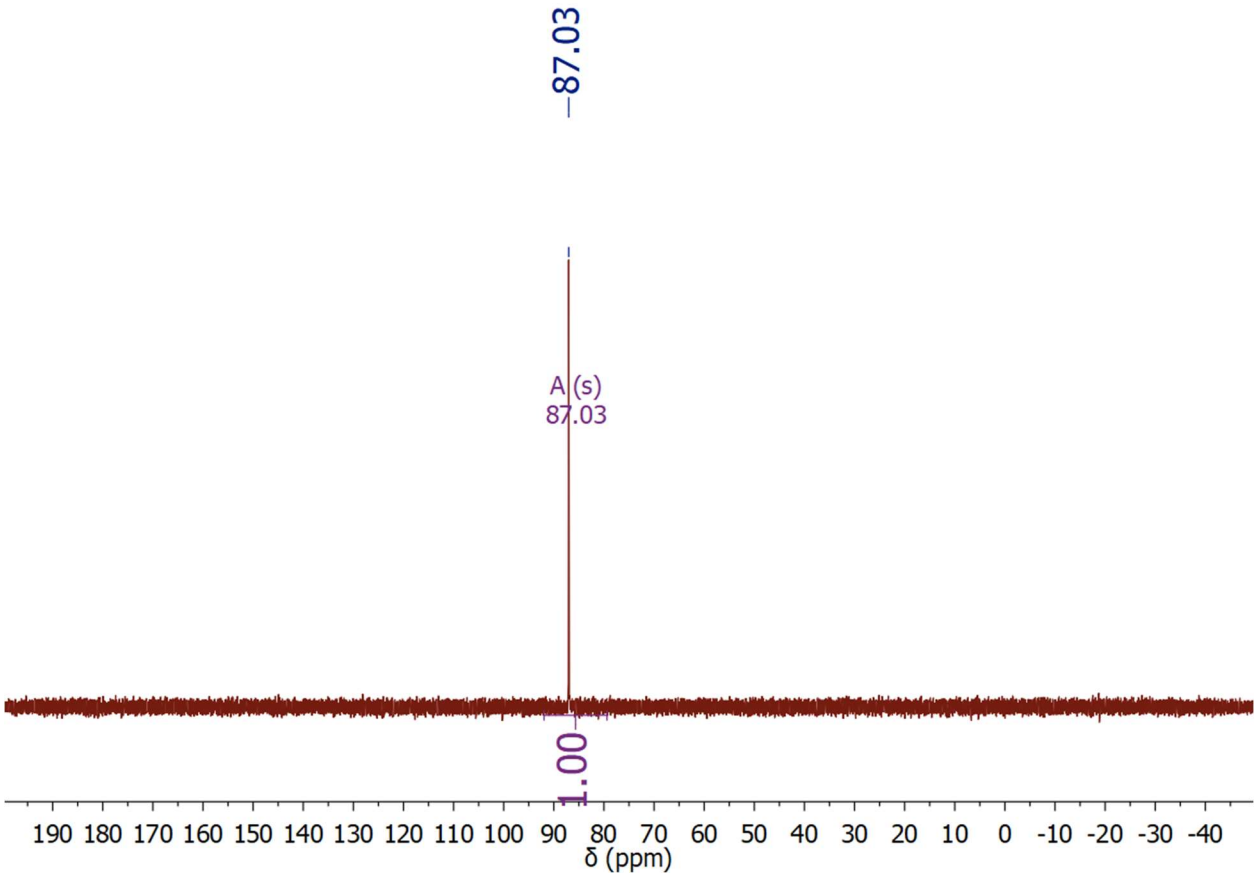

3.5 ^{57}Fe Mössbauer Spectroscopy:

Figure S32. [**6**]BAr^{F}_{4}, 80 K ^{57}Fe Mössbauer spectrum collected in the presence of a 50 mT magnetic field oriented parallel to the propagation of the γ-beam (frozen solution in Et_2O). δ = 0.16 mm/s, ΔE_Q = 1.75 mm/s for major species. $\Gamma_L = \Gamma_R$ = + 0.50 mm/s.

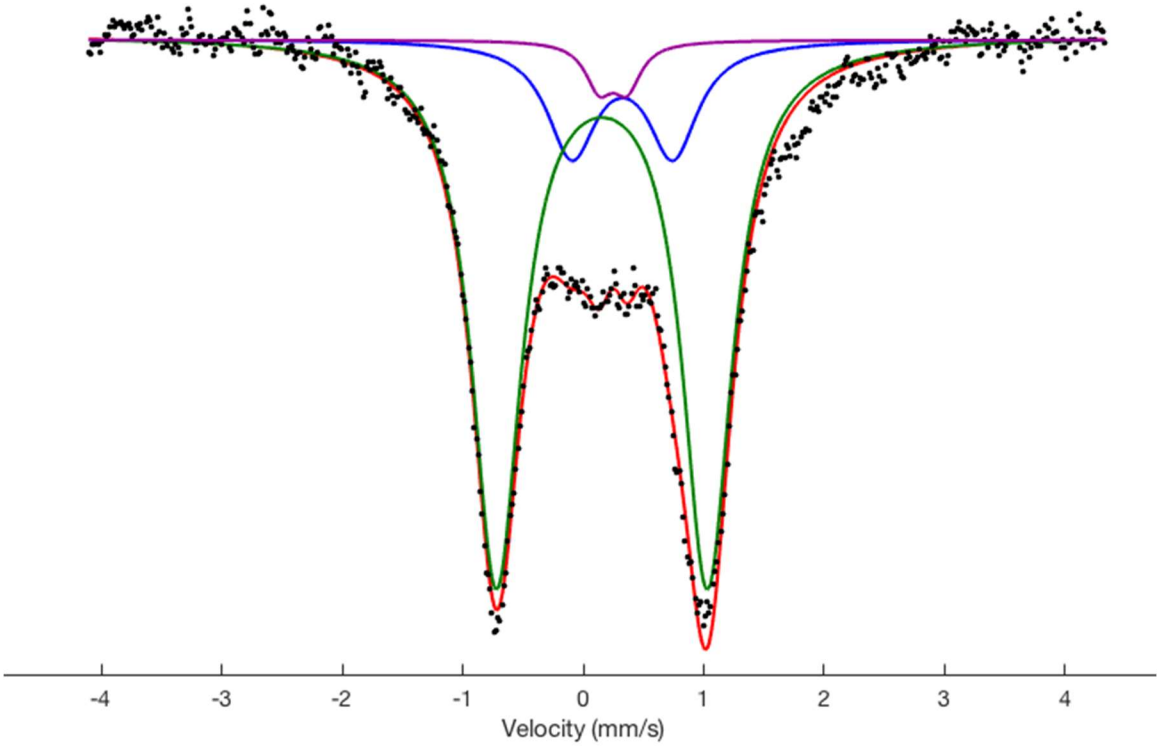

δ = 0.16 and ΔE_Q = 1.75 (81%)

δ = 0.33 and ΔE_Q = 0.84 (17%)

δ = 0.24 and ΔE_Q = 0.23 (3%)

3.6 UV-Visible Spectroscopy:

Figure S33. [**1**]BAr^F_4, UV-Visible spectrum showing stability over 24 h, 2-MeTHF, 298 K (λ = 396, 506 nm)

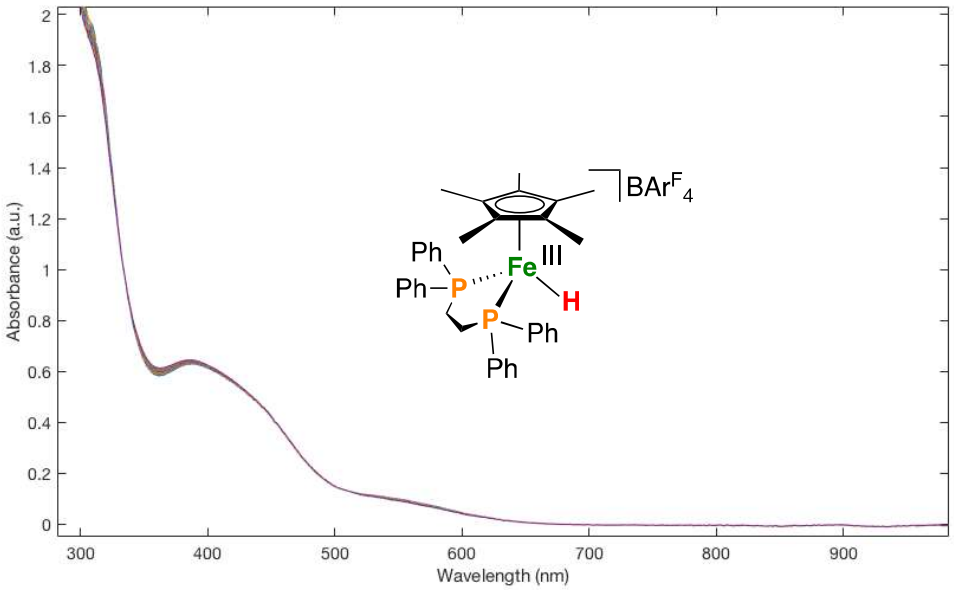

Figure S34. *endo*-**3** and *exo*-**3**, UV-Visible spectrum (2-MeTHF, 298 K, 1 cm cell). *endo*-**3**: λ = 450 {1130}, *exo*-**3**: λ = 441 {1850}.

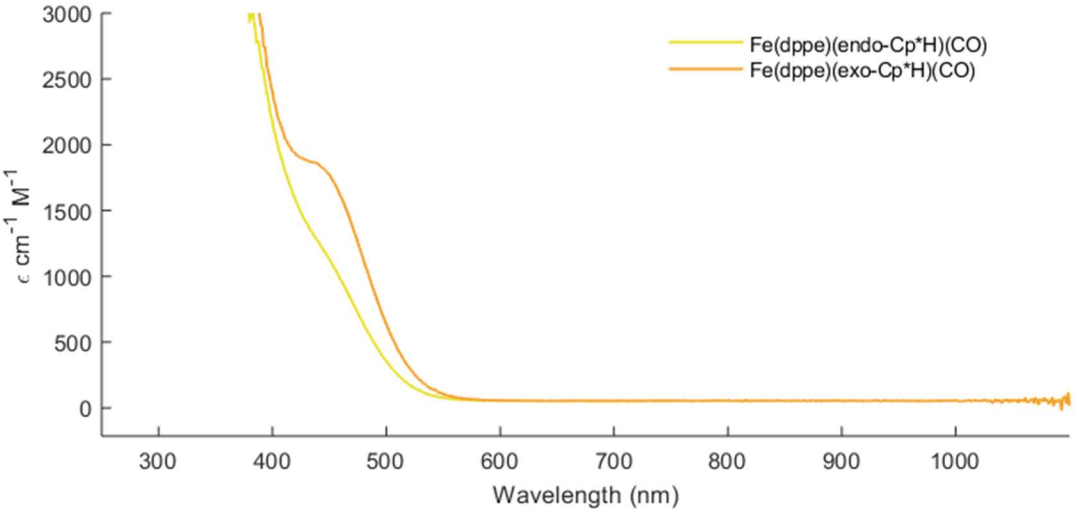

Figure S35. *endo*-[**3**]$^+$ and *exo*-[**3**]$^+$, UV-Visible spectrum (2-MeTHF, 218 K, 1 cm cell). *endo*-[**3**]$^+$: λ = 891 {252}, 712 {425}, 459 {870}, 383 {1530}, *exo*-[**3**]$^+$: λ = 923 {130}, 767, {180}, 441 {1645}.

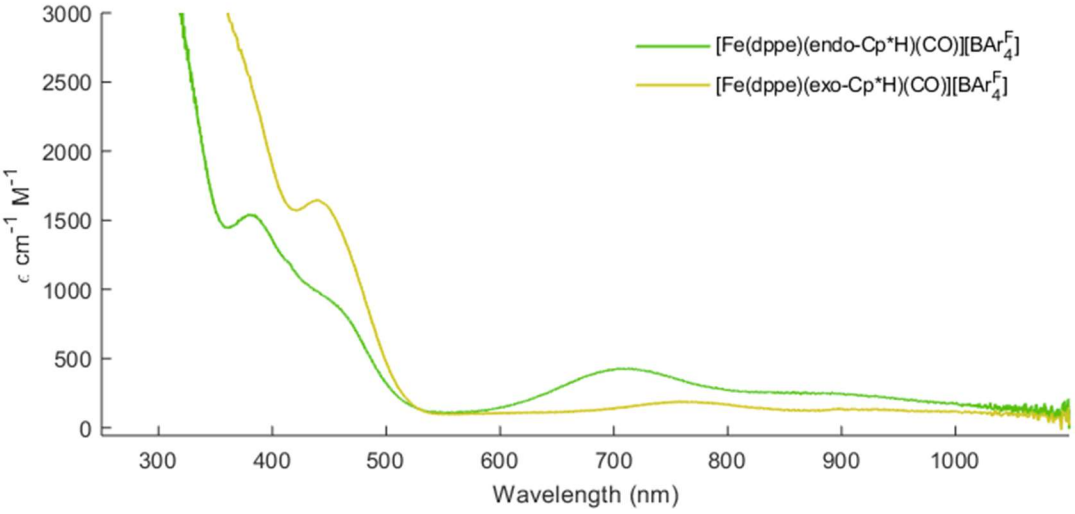

3.7 EPR Spectroscopy

3.7.1 CW-EPR:

Figure S36. CW X-band EPR data for **[1]**$^{+}$ (2-MeTHF, 77 K; MW frequency = 9.36 GHz; MW power = 20 μW; modulation amplitude = 10 mT; conversion time = 10.24 ms). Simulation parameters: g = [2.352, 2.041, 1.992]; A(^{31}P$_1$) = [88, 82, 79] MHz; A(^{31}P$_2$) = [82, 71, 76] MHz. For details, see: Drover, M. W.; Schild, D. J.; Oyala, P. H.; Peters, J. C. *Angew. Chem. Int. Ed.* **2019**, *58*, 15504.

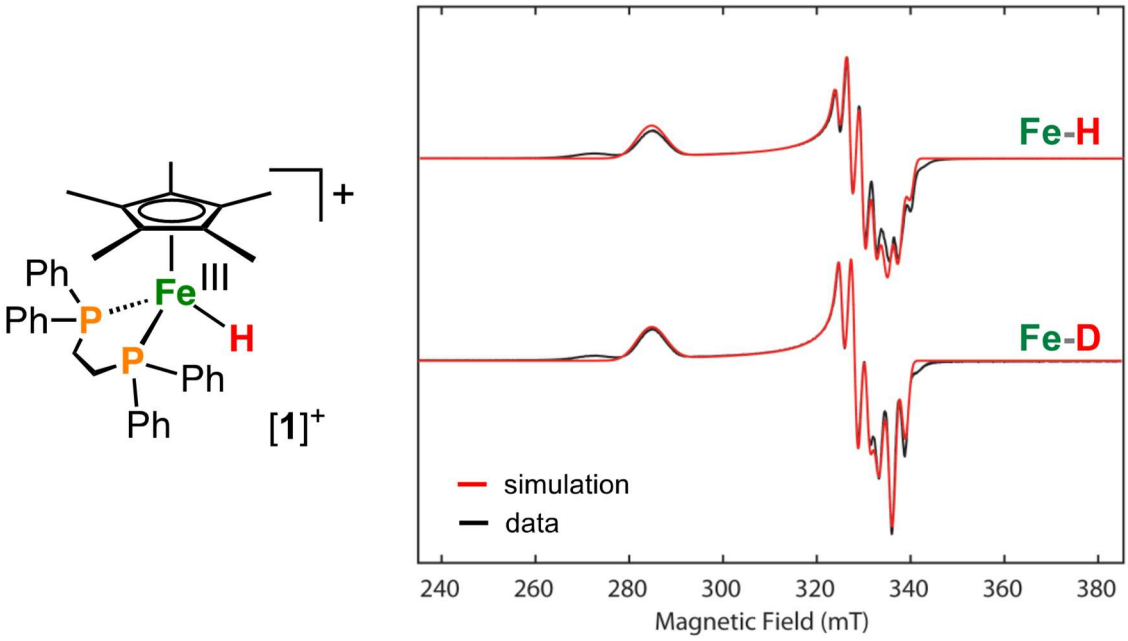

Figure S37. CW X-band EPR data for *endo*-[**3-H/D**]$^+$ (2-MeTHF, 77 K; MW frequency = 9.37 GHz; MW power = 2 mW; modulation amplitude = 10.0 mT; conversion time = 5.12 ms). Parameters: g = [2.085, 2.039, 2.004]; A($^{31}P_1$) = [72, 59, 58] MHz, A($^{31}P_2$) = [49, 42, 51] MHz.

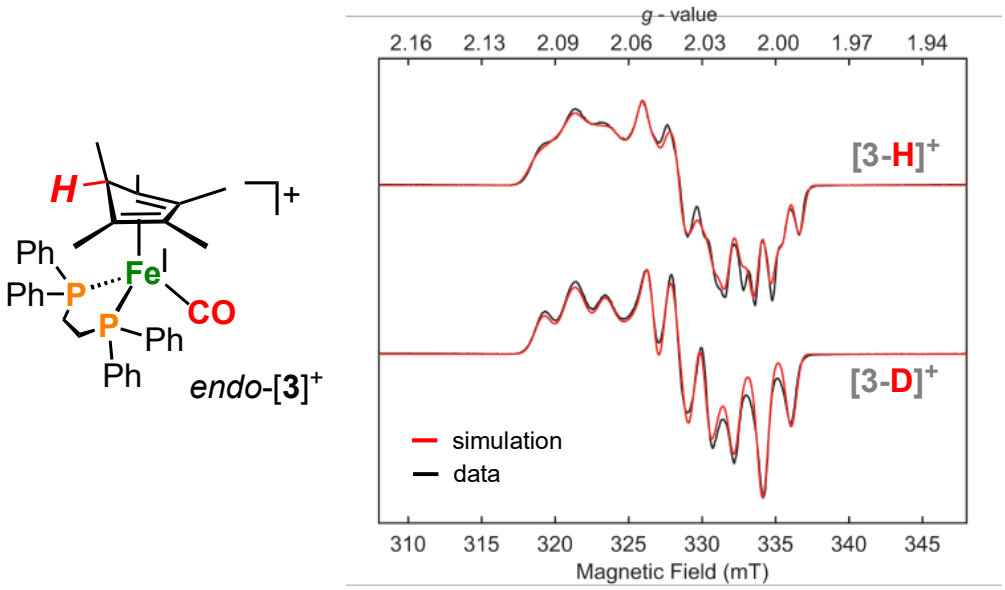

Figure S38. CW X-band EPR data for *endo*-[**4-H/D**]$^+$ (2-MeTHF, 77 K; MW frequency = 9.37 GHz; MW power = 2 mW; modulation amplitude = 10 mT; conversion time = 10.24 ms). Parameters: g = [2.132, 2.042, 2.004]; A($^{31}P_1$) = [75, 35, 54] MHz, A($^{31}P_2$) = [76, 64, 64] MHz. ** = traces of [**1**]$^+$.

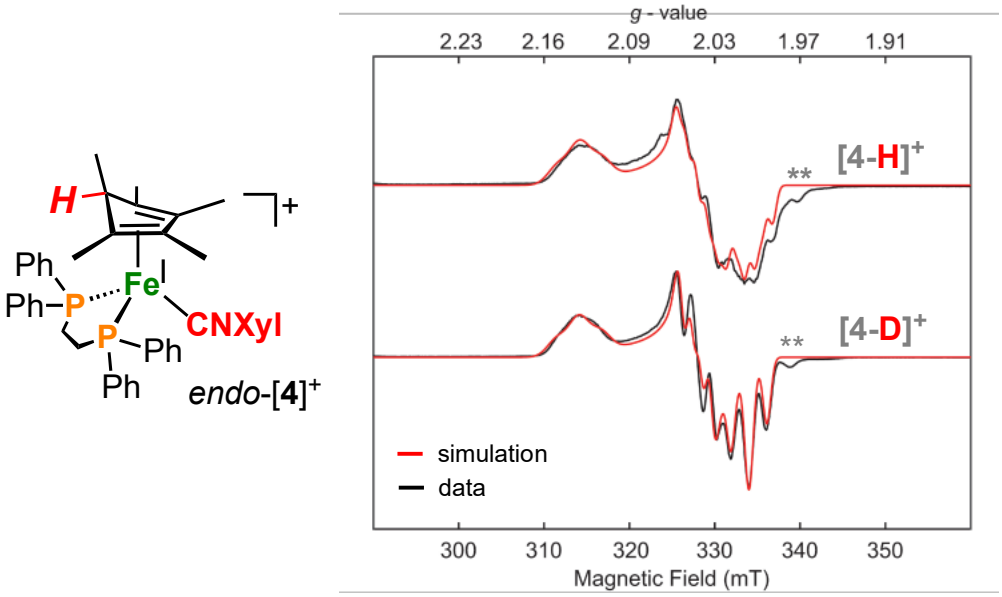

Figure S39. CW X-band EPR data for *exo*-[**3-H**]$^+$ and *exo*-[**3-D**]$^+$ (2-MeTHF, 77 K, 9.33 GHz; MW power = 6.44 mW; modulation amplitude = 2.0 mT; conversion time = 20.48 ms). **Parameters:** g = [2.116, 2.073, 1.997]; A(^{31}P$_1$) = [96, 88, 47] MHz; A(^{31}P$_2$) = [78, 75, 63] MHz; *A*(^{1}H) = ± [85, 84, 83] MHz, HStrain = [70, 22, 22] MHz for conformer **A** (0.6 weight) and g = [2.093, 2.045, 2.013]; A(^{31}P$_1$) = [46, 44, 15] MHz; A(^{31}P$_2$) = [70, 64, 64] MHz; *A*(^{1}H) = ± [76, 74, 70] MHz, HStrain = [70, 22, 22] MHz for conformer **B** (0.4 weight).

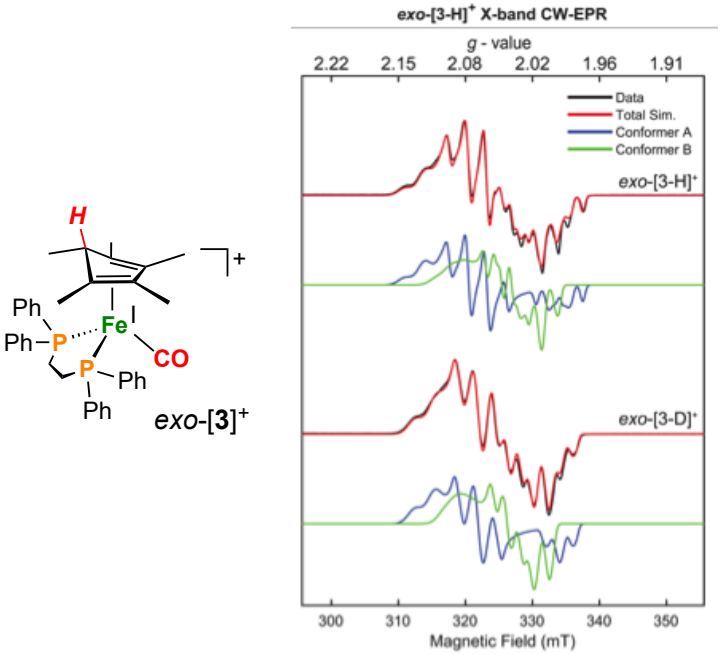

Figure S40. EPR sample of [**4-H**]$^{+}$ frozen at 77 K.

3.7.2 X-band Davies ENDOR:

Figure S41. Field-dependent X-band ^{31}P Davies ENDOR of *endo*-[**3-D**]$^{+}$ (black), with simulations of ^{31}P hyperfine couplings overlaid (total ^{31}P simulation (red), $^{31}P_1$, (green), $^{31}P_2$ (blue)). Simulation parameters: g = [2.085, 2.039, 2.004]; A($^{31}P_1$) = [72, 59, 58] MHz, A($^{31}P_2$) = [49, 42, 51] MHz. Acquisition parameters: temperature = 30 K; MW frequency = 9.717 GHz; MW pulse length ($\pi/2$, π) = 40 ns, 80 ns; tau = 200 ns; RF pulse length = 15 μs; shot repetition time = 4 ms.

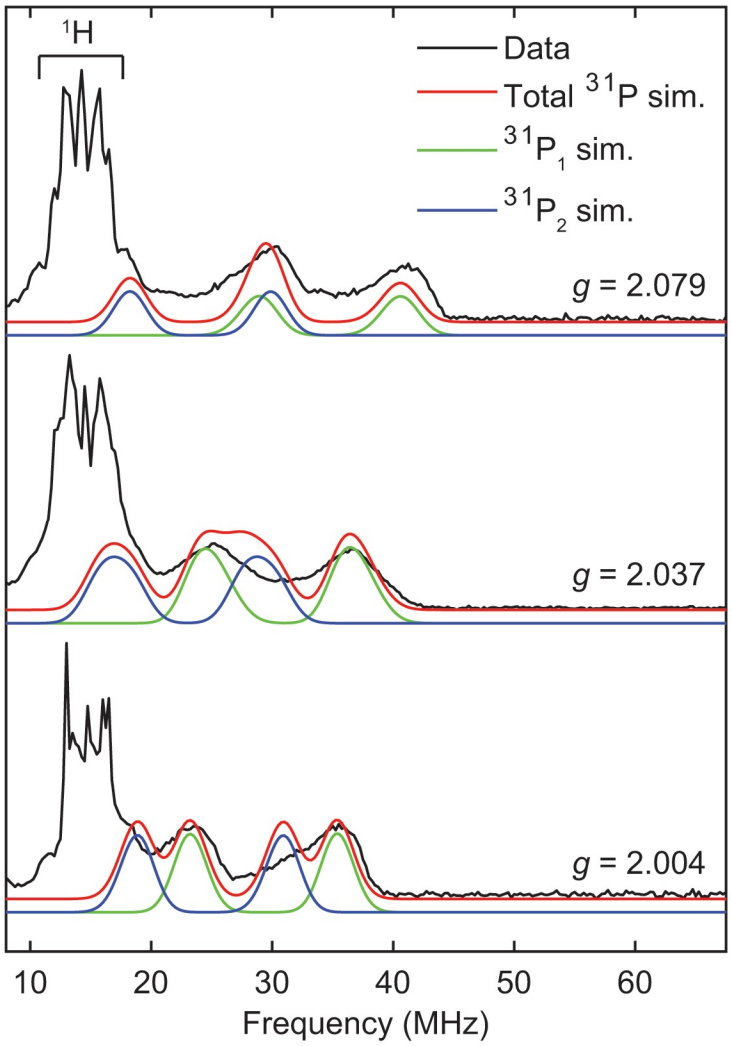

Figure S42. Field-dependent X-band ^{31}P Davies ENDOR of *exo*-[**3-D**]$^{+}$ (black), with simulations of ^{31}P hyperfine couplings overlaid (total ^{31}P simulation (red), $^{31}P_1$ conformer **A**, (dark blue), $^{31}P_2$ conformer **A** (turquoise), $^{31}P_1$ conformer **B**, (forest green), $^{31}P_2$ conformer **B** (lime green). Simulation parameters for conformer **A**: g = [2.116, 2.073, 1.997]; A($^{31}P_1$) = [96, 88, 47] MHz, A($^{31}P_2$) = [78, 75, 63] MHz. Simulation parameters for conformer **B**: g = [2.093, 2.045, 2.013]; A($^{31}P_1$) = [46, 44, 15] MHz, A($^{31}P_2$) = [70, 64, 64] MHz. Acquisition parameters: temperature = 20 K; MW frequency = 9.734 GHz; MW pulse length ($\pi/2$, π) = 40 ns, 80 ns; tau = 200 ns; RF pulse length = 15 μs; shot repetition time = 4 ms.

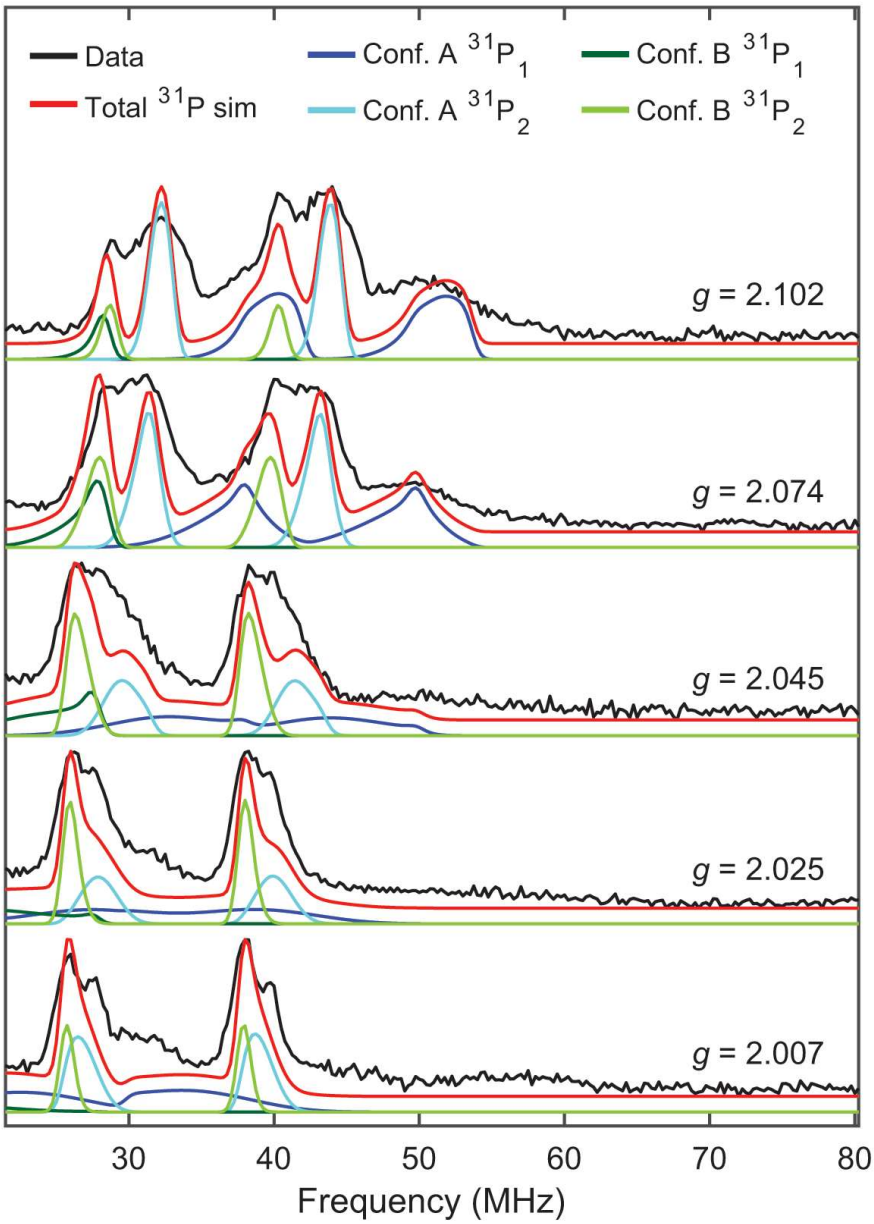

Figure S43. Field-dependent X-band Davies ENDOR spectra of *exo*-[**3-H**]$^+$ (black) and *exo*-[**3-D**]$^+$ (black). Acquisition parameters: temperature = 20 K; microwave frequency = 9.734 GHz; MW pulse length ($\pi/2$, π) = 40 ns, 80 ns; τ = 200; RF pulse length π_{RF} = 15 μs; T_{RF} = 2 μs; shot repetition time (srt) = 4 ms. Asterisk at ~ 4 MHz indicates an RF artifact.

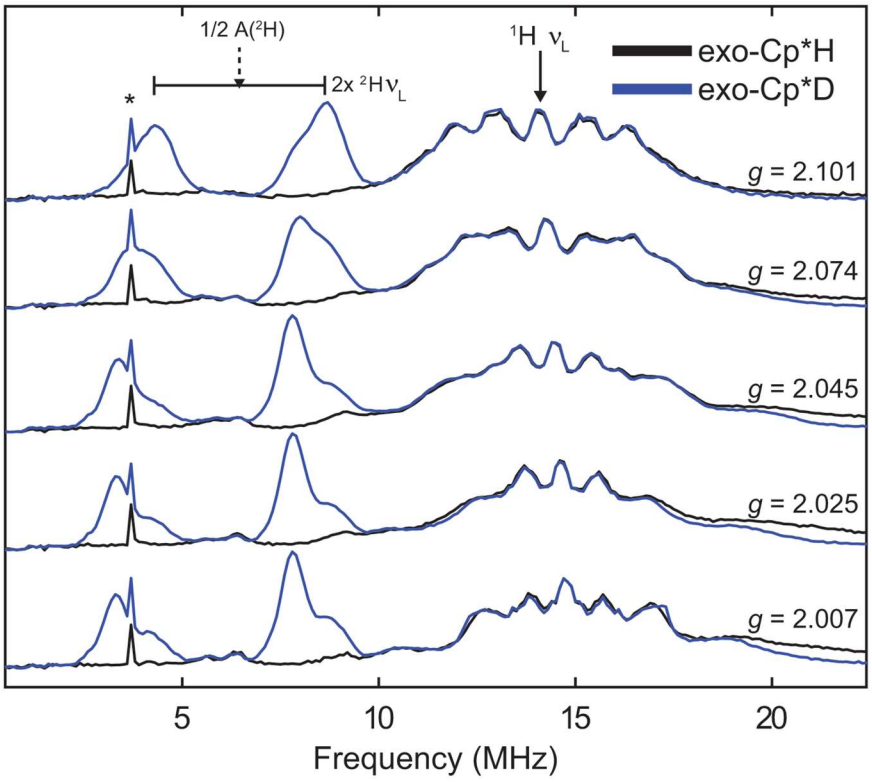

Figure S44. Field-dependent X-band ^{31}P Davies ENDOR of *endo*-[**4-D**]$^{+}$ (black), with simulations of ^{31}P hyperfine couplings overlaid (total ^{31}P simulation (red), $^{31}P_1$, (green), $^{31}P_2$ (blue)). Simulation parameters: g = [2.132, 2.042, 2.004]; A($^{31}P_1$) = [75, 35, 54] MHz, A($^{31}P_2$) = [76, 64, 64] MHz. Acquisition parameters: temperature = 20 K; MW frequency = 9.716 GHz; MW pulse length ($\pi/2$, π) = 40 ns, 80 ns; tau = 200 ns; RF pulse length = 15 μs; shot repetition time = 4 ms.

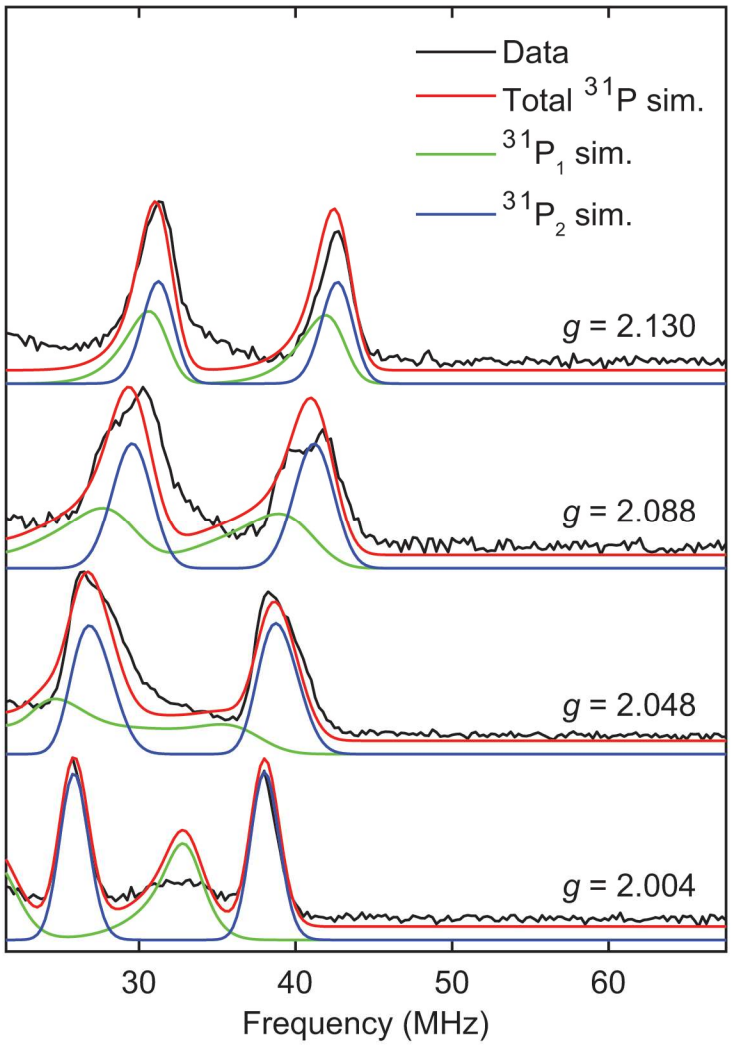

3.7.3 X-band HYSCORE:

Figure S45. Field-dependent X-band HYSCORE spectra of *endo*-[**3-H**]$^+$ (top panels) *endo*-[**3-D**]$^+$ (middle panels) and ^{1}H-^{2}H difference HYSCORE spectra (bottom panels). Acquisition parameters: temperature = 30 K; microwave frequency = 9.717 GHz; MW pulse length ($\pi/2$, π) = 8 ns, 16 ns; τ = 140 ns (g = 2.079), 138 ns (g = 2.037); 138 ns (g = 2.004); $t_1 = t_2$ = 100 ns; $\Delta t_1 = \Delta t_2$ = 12 ns; shot repetition time (srt) = 2 ms.

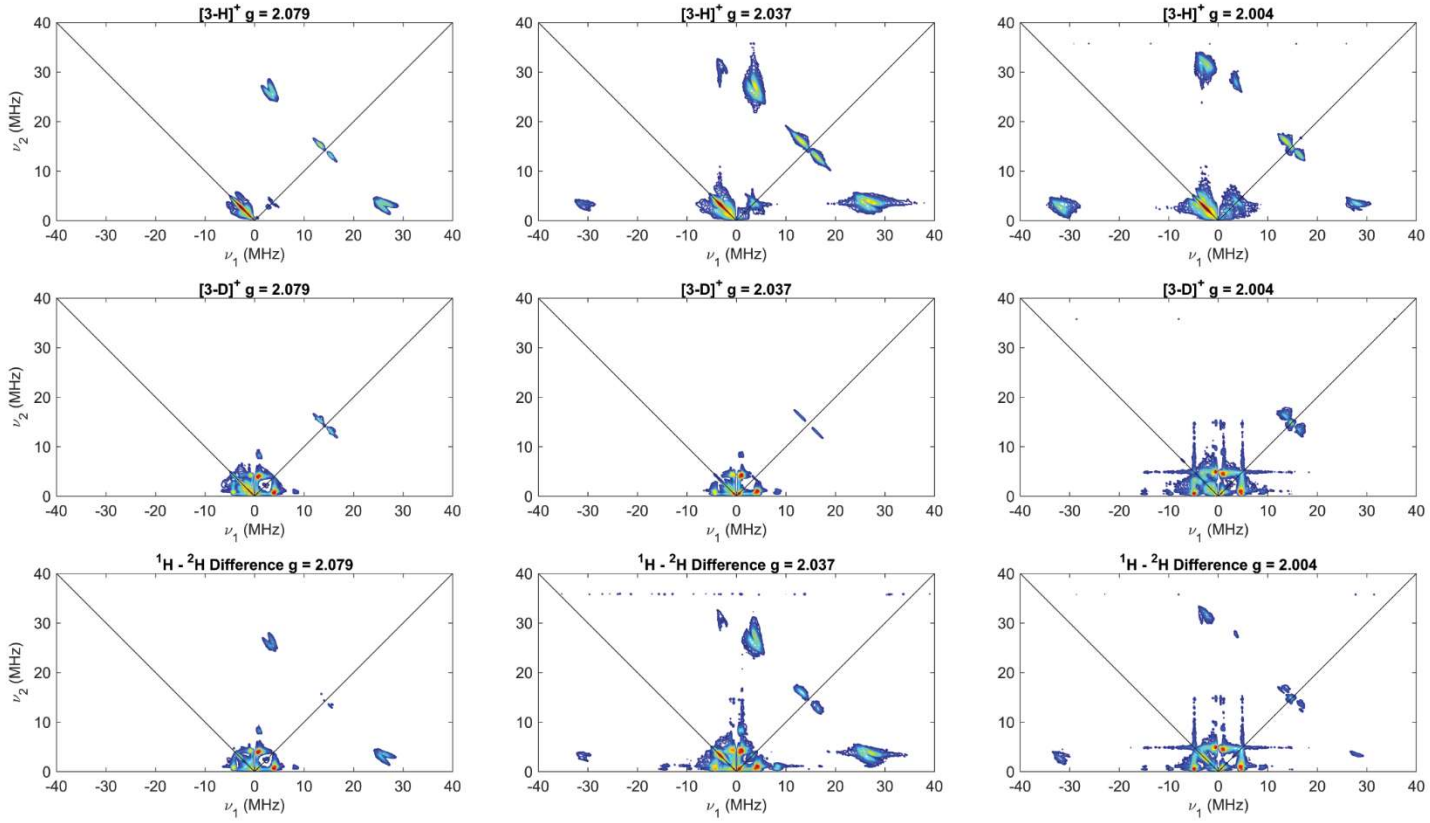

Figure S46. Field-dependent X-band HYSCORE spectra of *endo*-[**4-H**]$^+$ (top panels) *endo*-[**4-D**]$^+$ (middle panels) and ^{1}H-^{2}H difference HYSCORE spectra (bottom panels). Acquisition parameters: temperature = 30 K; microwave frequency = 9.717 GHz; MW pulse length ($\pi/2$, π) = 8 ns, 16 ns; τ = 144 ns (g = 2.130), 142 ns (g = 2.088); 138 ns (g = 2.048); 138 ns (g = 2.004); $t_1 = t_2$ = 100 ns; $\Delta t_1 = \Delta t_2$ = 12 ns; shot repetition time (srt) = 2 ms.

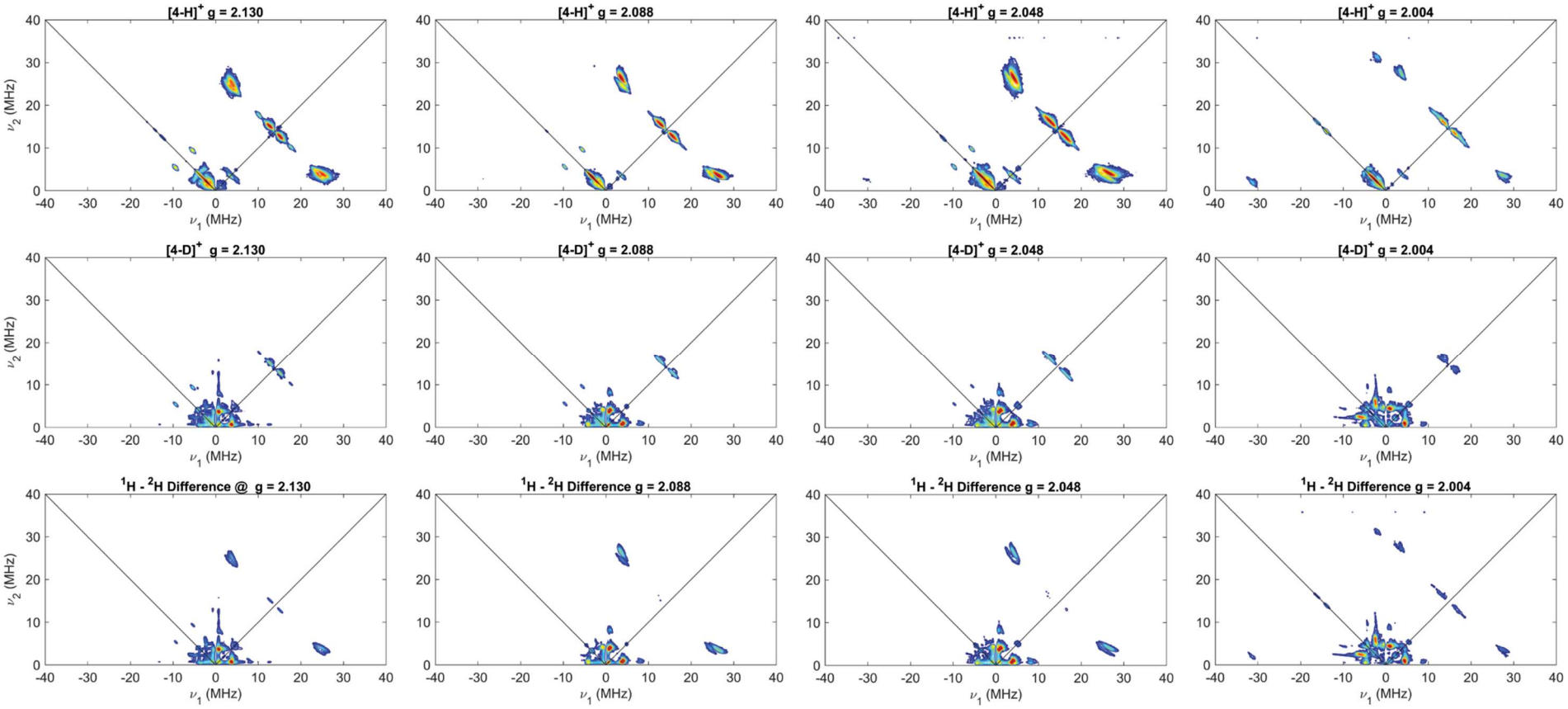

Figure S47. X-band HYSCORE spectra of *endo*-[**3-H**]$^+$ and *endo*-[**3-D**]$^+$ (top panels) and ^{1}H/^{2}H HYSCORE simulation spectra (bottom panels) at a magnetic field corresponding to g = 2.079. Acquisition parameters: temperature = 30 K; microwave frequency = 9.717 GHz; Magnetic field = 334 mT; MW pulse length ($\pi/2$, π) = 8 ns, 16 ns; τ = 140 ns, $t_1 = t_2$ = 100 ns; $\Delta t_1 = \Delta t_2$ = 12 ns; shot repetition time (srt) = 2 ms.

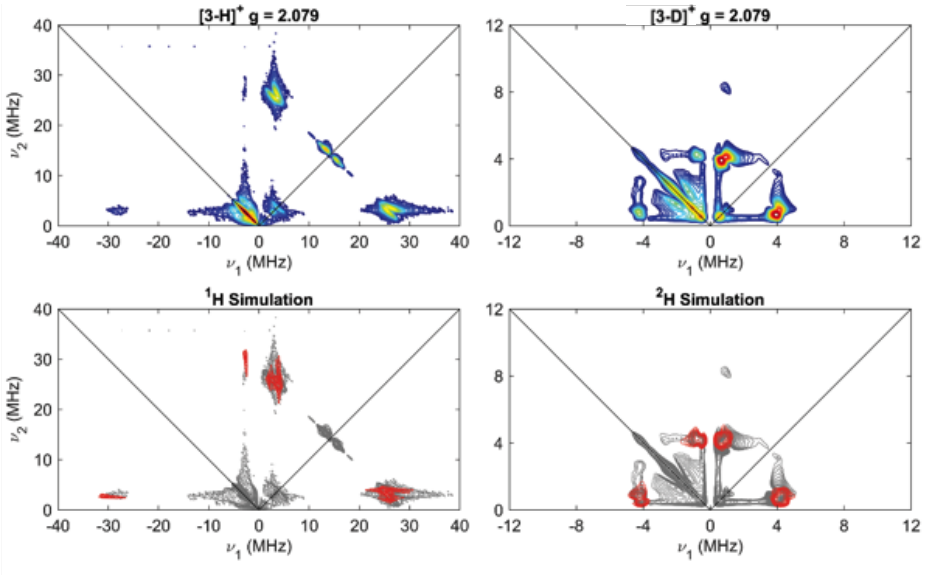

Figure S48. X-band HYSCORE spectra of *endo*-[**3-H**]$^+$ and *endo*-[**3-D**]$^+$ (top panels) and ^{1}H/^{2}H HYSCORE simulation spectra (bottom panels) at a magnetic field corresponding to g = 2.037. Acquisition parameters: temperature = 30 K; microwave frequency = 9.717 GHz; Magnetic field = 340.8 mT; MW pulse length ($\pi/2$, π) = 8 ns, 16 ns; τ = 138 ns, $t_1 = t_2$ = 100 ns; $\Delta t_1 = \Delta t_2$ = 12 ns; shot repetition time (srt) = 2 ms.

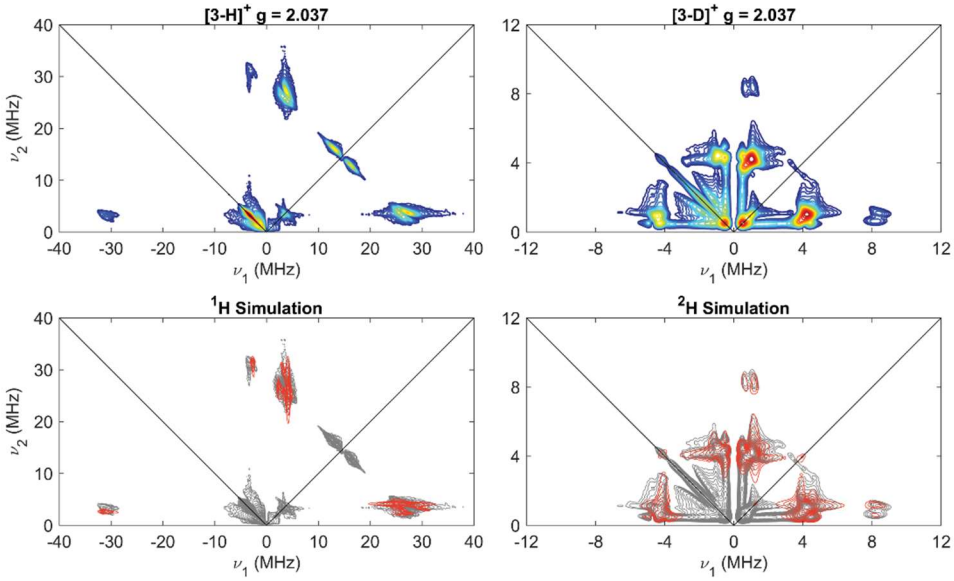

Figure S49. X-band HYSCORE spectra of *endo*-[**3-H**]$^+$ and *endo*-[**3-D**]$^+$ (top panels) and ^{1}H/^{2}H HYSCORE simulation spectra (bottom panels) at a magnetic field corresponding to g = 2.004. Acquisition parameters: temperature = 30 K; microwave frequency = 9.717 GHz; Magnetic field = 346.5 mT; MW pulse length ($\pi/2$, π) = 8 ns, 16 ns; τ = 138 ns, $t_1 = t_2$ = 100 ns; $\Delta t_1 = \Delta t_2$ = 12 ns; shot repetition time (srt) = 2 ms.

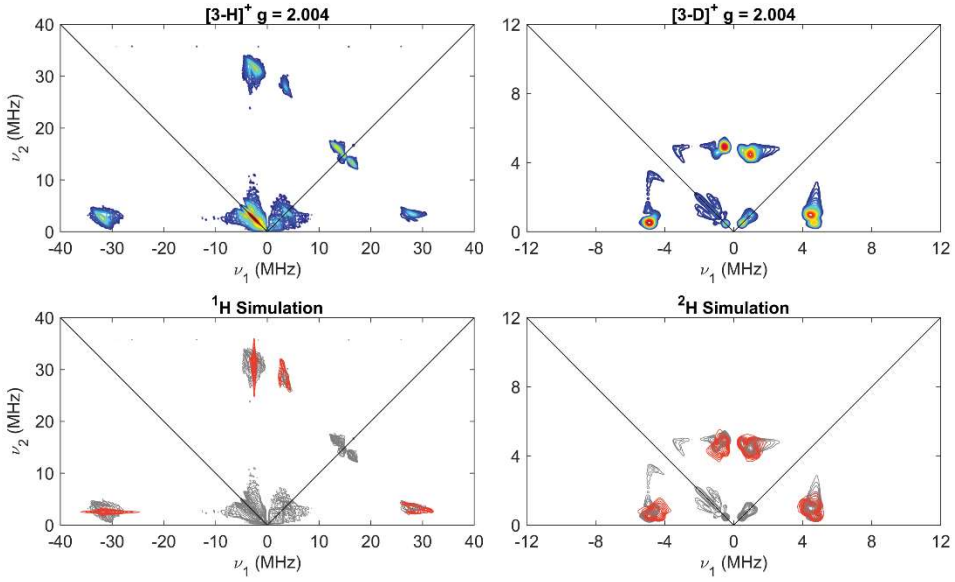

Figure S50. Field-dependent X-band HYSCORE spectra of *exo*-[**3-D**]$^+$ (top panels) and ^{2}H HYSCORE simulations (bottom panels) of conformations A (blue) and B (green) (bottom panels). Acquisition parameters: temperature = 25 K; microwave frequency = 9.734 GHz; Magnetic field = 330.8 mT (g = 2.102), 340.0 mT (g = 2.045), 346.5 mT (g = 2.007); MW pulse length ($\pi/2$, π) = 8 ns, 16 ns; τ = 142 ns (g = 2.102), τ = 138 ns (g = 2.045), τ = 136 ns (g = 2.007); $t_1 = t_2$ = 100 ns; $\Delta t_1 = \Delta t_2$ = 12 ns; shot repetition time (srt) = 2 ms.

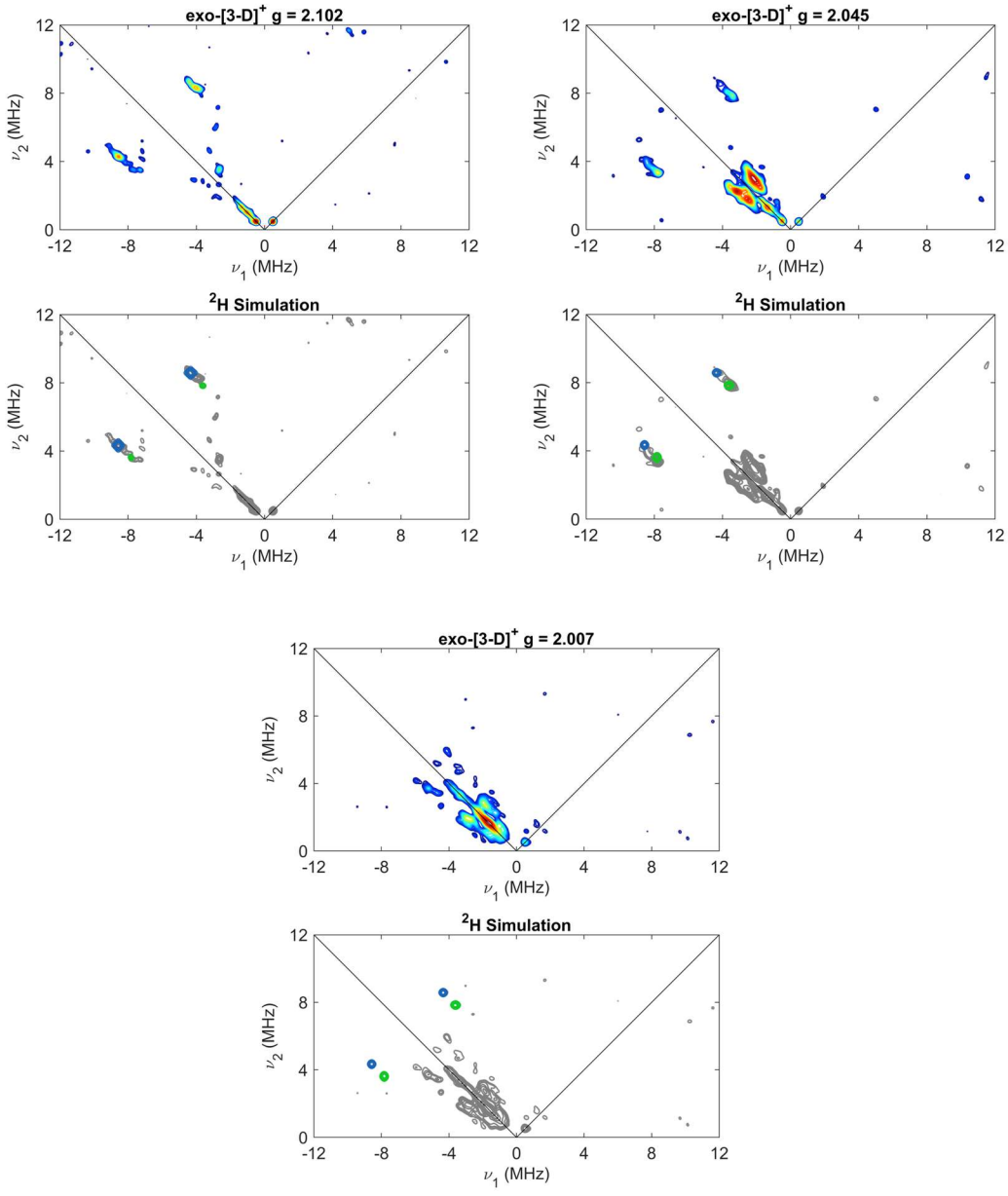

Figure S51. X-band HYSCORE spectra of *endo*-[**4-H**]$^+$ and *endo*-[**4-D**]$^+$ (top panels) and ^{1}H /^{2}H (red) and ^{14}N (green) simulations overlaid (bottom panels) at a magnetic field corresponding to g = 2.130. Acquisition parameters: temperature = 30 K; microwave frequency = 9.717 GHz; MW pulse length (π/2, π) = 8 ns, 16 ns; τ = 144 ns; Magnetic Field = 326.0 mT; $t_1 = t_2$ = 100 ns; $\Delta t_1 = \Delta t_2$ = 12 ns; shot repetition time (srt) = 2 ms.

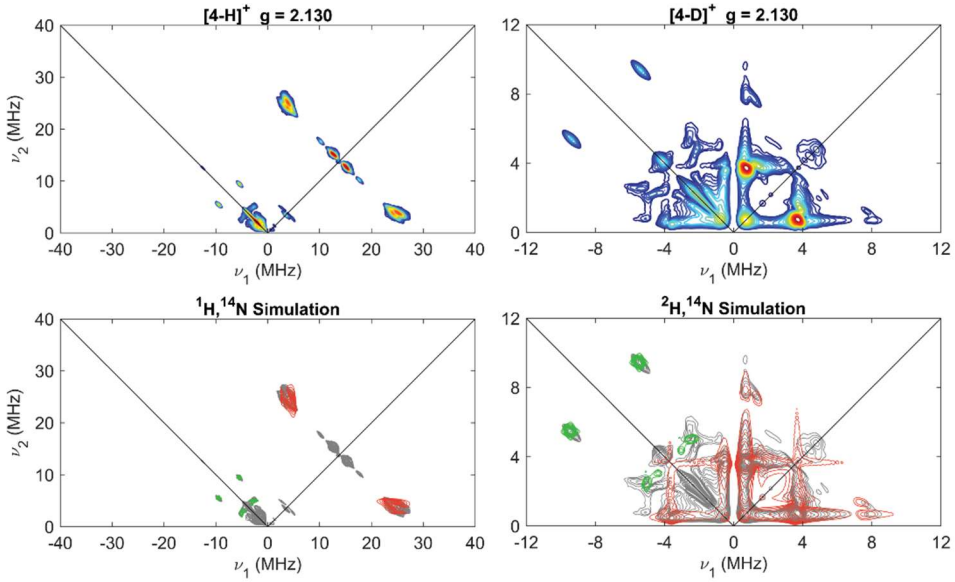

Figure S52. X-band HYSCORE spectra of *endo*-[**4-H**]$^+$ and *endo*-[**4-D**]$^+$ (top panels) and ^{1}H /^{2}H (red) and ^{14}N (green) simulations overlaid (bottom panels) at a magnetic field corresponding to g = 2.088. Acquisition parameters: temperature = 30 K; microwave frequency = 9.717 GHz; MW pulse length (π/2, π) = 8 ns, 16 ns; τ = 142 ns; Magnetic Field = 332.5 mT; $t_1 = t_2$ = 100 ns; $\Delta t_1 = \Delta t_2$ = 12 ns; shot repetition time (srt) = 2 ms.

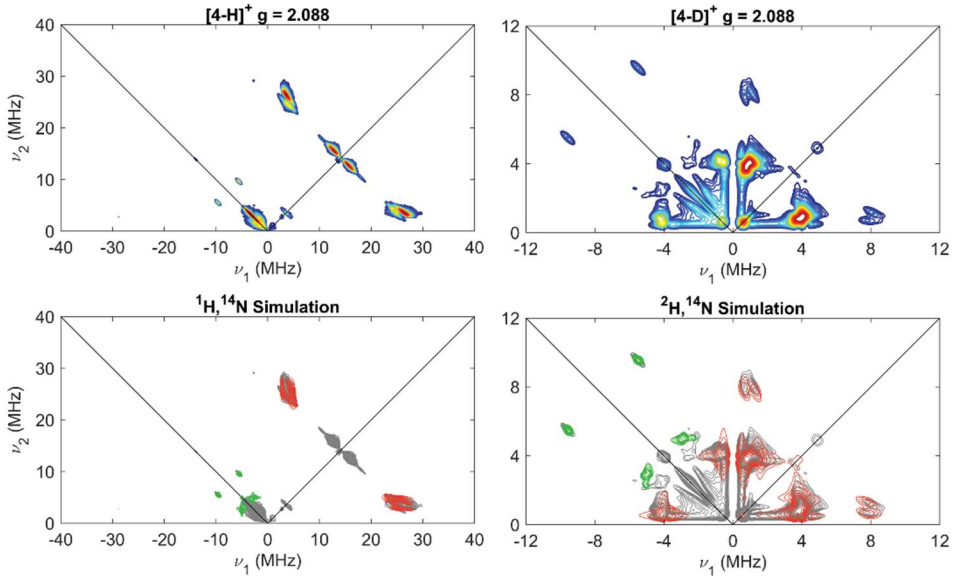

Figure S53. X-band HYSCORE spectra of *endo*-[**4-H**]$^+$ and *endo*-[**4-D**]$^+$ (top panels) and ^{1}H /^{2}H (red) and ^{14}N (green) simulations overlaid (bottom panels) at a magnetic field corresponding to g = 2.048 Acquisition parameters: temperature = 30 K; microwave frequency = 9.717 GHz; MW pulse length (π/2, π) = 8 ns, 16 ns; τ = 138 ns; Magnetic Field = 339.0 mT; $t_1 = t_2$ = 100 ns; $\Delta t_1 = \Delta t_2$ = 12 ns; shot repetition time (srt) = 2 ms.

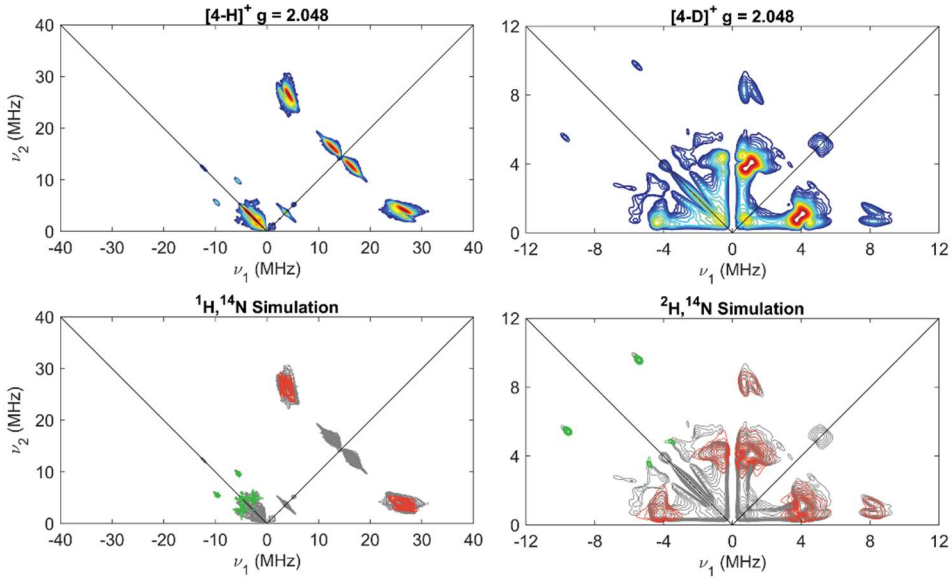

Figure S54. X-band HYSCORE spectra of *endo*-[**4-H**]$^+$ and *endo*-[**4-D**]$^+$ (top panels) and ^{1}H /^{2}H (red) and ^{14}N (green) simulations overlaid (bottom panels). Intense features in the (+,-) quadrant of the HYSCORE spectrum of *endo*-[**4-D**]+ are due to contribution of a small amount of residual starting [**1-D**]$^+$. Acquisition parameters: temperature = 30 K; microwave frequency = 9.717 GHz; MW pulse length (π/2, π) = 8 ns, 16 ns; τ = 138 ns; Magnetic Field = 346.5 mT; $t_1 = t_2$ = 100 ns; $\Delta t_1 = \Delta t_2$ = 16 ns; shot repetition time (srt) = 2 ms.

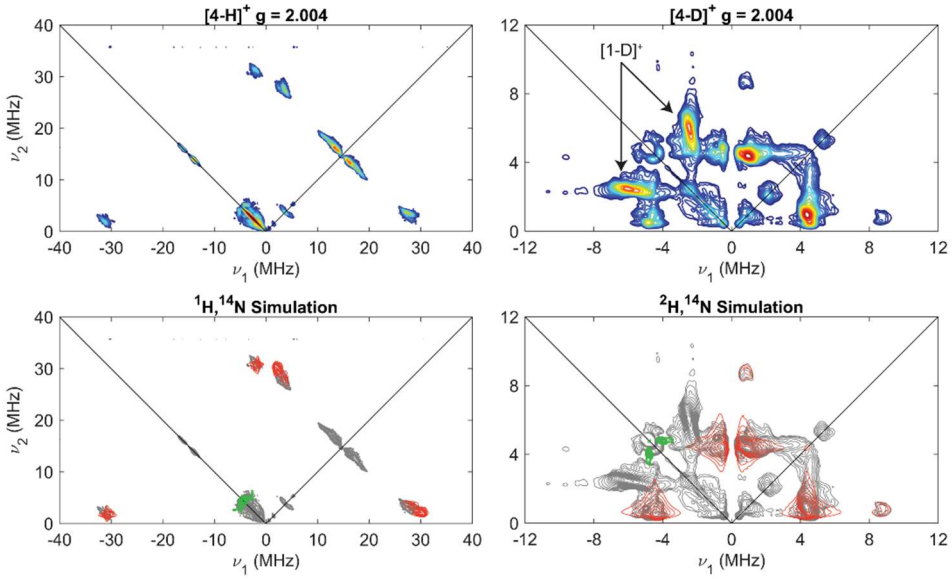

3.8 Electrochemistry

Figure S55. Cyclic voltammogram of *endo*-**3**, showing a reversible Fe^{0}/Fe^{1+} feature at E_{ox} = -0.81 V (versus Fc/Fc^{+}).

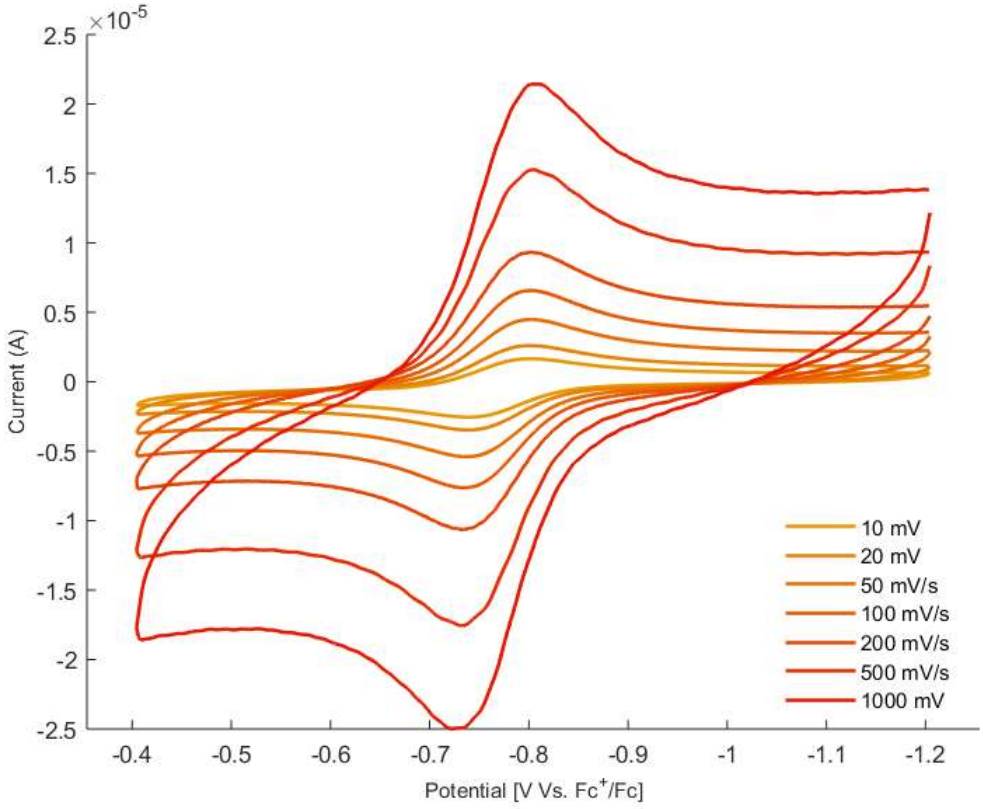

Figure S56. Cyclic voltammogram of *exo*-**3**, showing the Fe^0/Fe^{1+} feature become more reversable upon increasing the scan rate from 1 V/s to 100 V/s at E_{ox} = -0.70 V (versus Fc/Fc^+).

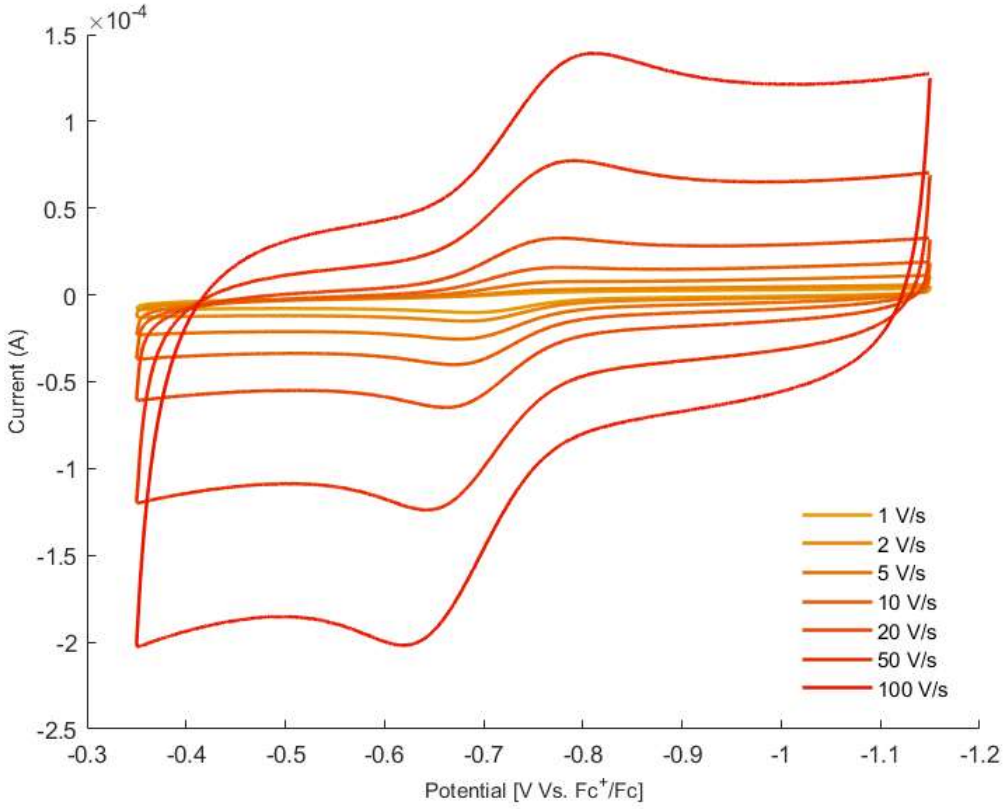

4. Crystallographic details

All crystals were mounted on a glass fiber loop. All measurements were made using graphite-monochromated Mo or Cu K_α radiation (λ = 0.71073 or 1.54178 Å) radiation on a Bruker AXS D8 VENTURE KAPPA diffractometer coupled to a PHOTON 100 CMOS detector. The structures were solved by direct methods[8] and refined by full-matrix least-squares procedures on F2 (SHELXL-2013)[6] using the OLEX2 interface.[9] All hydrogen atoms were placed in calculated positions. Non-hydrogen atoms were refined anisotropically.

endo-[**3**]BAr^{F_4} (L = CO): ISOR (0.001 0.001) was applied to a 2-methylcyclohexane moiety (C70-C76). Applications of these constraints improved data statistics. An A-level alert also persists for this molecule:

PLAT029_ALERT_3_A _diffrn_measured_fraction_theta_full value Low . 0.938 Why?

Author Response: This crystal has many weak reflections at higher values of 2theta (it is weakly diffracting and small). That said, it more than corroborates the connectivity for this species.

[**6**]BAr^{F_4} (*L* = CNXyl): Rotational disorder about two of the -CF_3 groups of the BAr^{F_4-} counterion was modeled F1/F2/F3 [46/54] and F7/F8/F9 [51/49]. RIGU was applied to two pentane solvent molecules [C77-C87] and ISOR (0.01 0.01) was applied to F1/F2/F3 and F7/F8/F9. Applications of these constraints improved data statistics.

[**7**]BAr^{F_4} (*L* = N_2): Rotational disorder about one of the -CF_3 groups of the BAr^{F_4-} counterion was modeled [50/50]. Application of these constraints improved data statistics.

CCDC **1943147-1943149** and **2021150-2021151** contains the supplementary crystallographic data for this paper. These data can be obtained free of charge from The Cambridge Crystallographic Data Centre via www.ccdc.cam.ac.uk/data_request/cif

Table S2. Crystallographic data for *endo*-**3** and *exo*-**3**.

Compound	*endo*-**3**	*exo*-**3**
Empirical formula	$C_{37}H_{40}FeOP_2$	$C_{37}H_{40}FeOP_2$
Formula weight	618.48	618.48
Temperature/K	100(2)	100(2)
Crystal system	Monoclinic	Monoclinic
Space group	$P2_1/n$	$P2_1/n$
a/Å	12.071(4)	12.161(5)
b/Å	19.165(3)	19.178(6)
c/Å	14.020(4)	13.920(5)
⍵/°	90	90
⍵/°	102.72(3)	104.70(2)
⍵/°	90	90
V/Å^3	3164.0(16)	3140.2(19)
Z	4	4
⍵/ g/cm^{-3}	1.298	1.308
⍵/ mm^{-1}	4.983	5.021
F(000)	1304.0	1304.0
Crystal size/ mm^3	0.12 × 0.11 × 0.09	0.32 × 0.19 × 0.14
Radiation	CuKα (λ = 1.54178)	CuKα (λ = 1.54178)
2θ range for data collection/°	7.942 to 163.416	8.024 to 149.76
Index ranges	-15 ≤ h ≤ 15, -24 ≤ k ≤ 23, -17 ≤ l ≤ 17	-13 ≤ h ≤ 15, -23 ≤ k ≤ 23, -17 ≤ l ≤ 17
Reflections collected	58389	102570
Independent reflections	6809 [R_{int} = 0.0727, R_{sigma} = 0.0358]	6420 [R_{int} = 0.0536, R_{sigma} = 0.0209]
Data/restraints/parameters	6809/0/375	6420/0/375
Goodness-of-fit on F^2	1.049	1.052
R [I>=2θ (I)] (R1, wR2)	R_1 = 0.0364, wR_2 = 0.0859	R_1 = 0.0272, wR_2 = 0.0754
R (all data) (R1, wR2)	R_1 = 0.0409, wR_2 = 0.0880	R_1 = 0.0276, wR_2 = 0.0757
Largest diff. peak/hole / (e Å^{-3})	0.55/-0.42	0.28/-0.39

$R1 = \Sigma \, ||F_o|-|F_c|| \, / \, \Sigma \, |F_o|$; $wR2 = [\Sigma(w(F_o^2 - F_c^2)^2) / \Sigma \, w(F_o^2)^2]^{1/2}$

Table S3. Crystallographic data for *endo*-[**3**]BAr^{F}_4 and [**6**]BAr^{F}_4.

Compound	*endo*-[**3**]BAr^{F}_4	[**6**]BAr^{F}_4 (*L* = CNXyl)
Empirical formula	$C_{76}H_{66}BF_{24}FeOP_2$	$C_{87}H_{84}BF_{24}FeNP_2$
Formula weight	1579.88	1728.15
Temperature/K	100(2)	100(2)
Crystal system	Triclinic	Triclinic
Space group	*P-1*	*P-1*
a/Å	14.148(6)	13.7115(6)
b/Å	16.393(4)	16.4188(8)
c/Å	17.640(7)	19.4299(9)
⍵/°	113.13(2)	86.338(2)
⍵/°	106.52(2)	69.671(2)
⍵/°	90.961(16)	88.504(2)
V/Å^3	3568(2)	4093.3(3)
Z	2	2
⍵/ g/cm^{-3}	1.470	1.402
⍵/ mm^{-1}	3.079	2.727
F(000)	1614.0	1780.0
Crystal size/ mm^3	0.23 × 0.13 × 0.11	0.21 × 0.16 × 0.14
Radiation	CuKα (λ = 1.54178)	CuKα (λ = 1.54178)
2θ range for data collection/°	5.744 to 161.046	4.858 to 161.348
Index ranges	-18 ≤ h ≤ 16, -20 ≤ k ≤ 14, -20 ≤ l ≤ 21	-17 ≤ h ≤ 17, -19 ≤ k ≤ 20, -24 ≤ l ≤ 24
Reflections collected	20853	204590
Independent reflections	13512 [R_{int} = 0.1012, R_{sigma} = 0.1579]	17660 [R_{int} = 0.0836, R_{sigma} = 0.0278]
Data/restraints/parameters	13512/42/940	17660/114/1112
Goodness-of-fit on F^2	1.086	1.049
R [I>=2θ (I)] (R1, wR2)	R_1 = 0.1289, wR_2 = 0.2951	R_1 = 0.0693, wR_2 = 0.2042
R (all data) (R1, wR2)	R_1 = 0.1857, wR_2 = 0.3381	R_1 = 0.0710, wR_2 = 0.2061
Largest diff. peak/hole / (e Å^{-3})	2.13/-0.92	2.12/-0.94

$R1 = \Sigma \, ||F_o|-|F_c|| \, / \, \Sigma \, |F_o|$; $wR2 = [\Sigma(w(F_o^2 - F_c^2)^2) / \Sigma \, w(F_o^2)^2]^{1/2}$

Table S4. Crystallographic data for [**7**]$BAr^{F}{}_{4}$.

Compound	[**7**]$BAr^{F}{}_{4}$ ($L = N_2$)
Empirical formula	$C_{68}H_{51}BF_{24}FeN_2P_2$
Formula weight	1480.70
Temperature/K	100(2)
Crystal system	Triclinic
Space group	*P-1*
a/Å	12.139(5)
b/Å	14.282(3)
c/Å	19.549(4)
⍵/°	91.970(16)
⍵/°	93.347(19)
⍵/°	106.142(18)
V/Å^3	3245.4(15)
Z	2
⍵/ g/cm^{-3}	1.515
⍵/ mm^{-1}	3.343
F(000)	1500.0
Crystal size/ mm^3	0.20 × 0.16 × 0.14
Radiation	CuKα (λ = 1.54178)
2θ range for data collection/°	6.452 to 162.704
Index ranges	-15 ≤ h ≤ 15, -18 ≤ k ≤ 18, -24 ≤ l ≤ 24
Reflections collected	175771
Independent reflections	14063 [R_{int} = 0.0447, R_{sigma} = 0.0204]
Data/restraints/parameters	14063/0/916
Goodness-of-fit on F^2	1.066
R [I>=2θ (I)] (R1, wR2)	R_1 = 0.0465, wR_2 = 0.1288
R (all data) (R1, wR2)	R_1 = 0.0510, wR_2 = 0.1331
Largest diff. peak/hole / (e Å^{-3})	1.12/-0.55

$R1 = \Sigma \, ||F_o|-|F_c|| \, / \, \Sigma \, |F_o|$; $wR2 = [\Sigma(w(F_o^2 - F_c^2)^2) / \Sigma \, w(F_o^2)^2]^{1/2}$

Figure S57. Thermal ellipsoid plot (50%) of **A**) *endo*-**3** and **B**) *exo*-**3** (*endo*-**3** had been reported previously[5], though the crystal structure was not obtained).

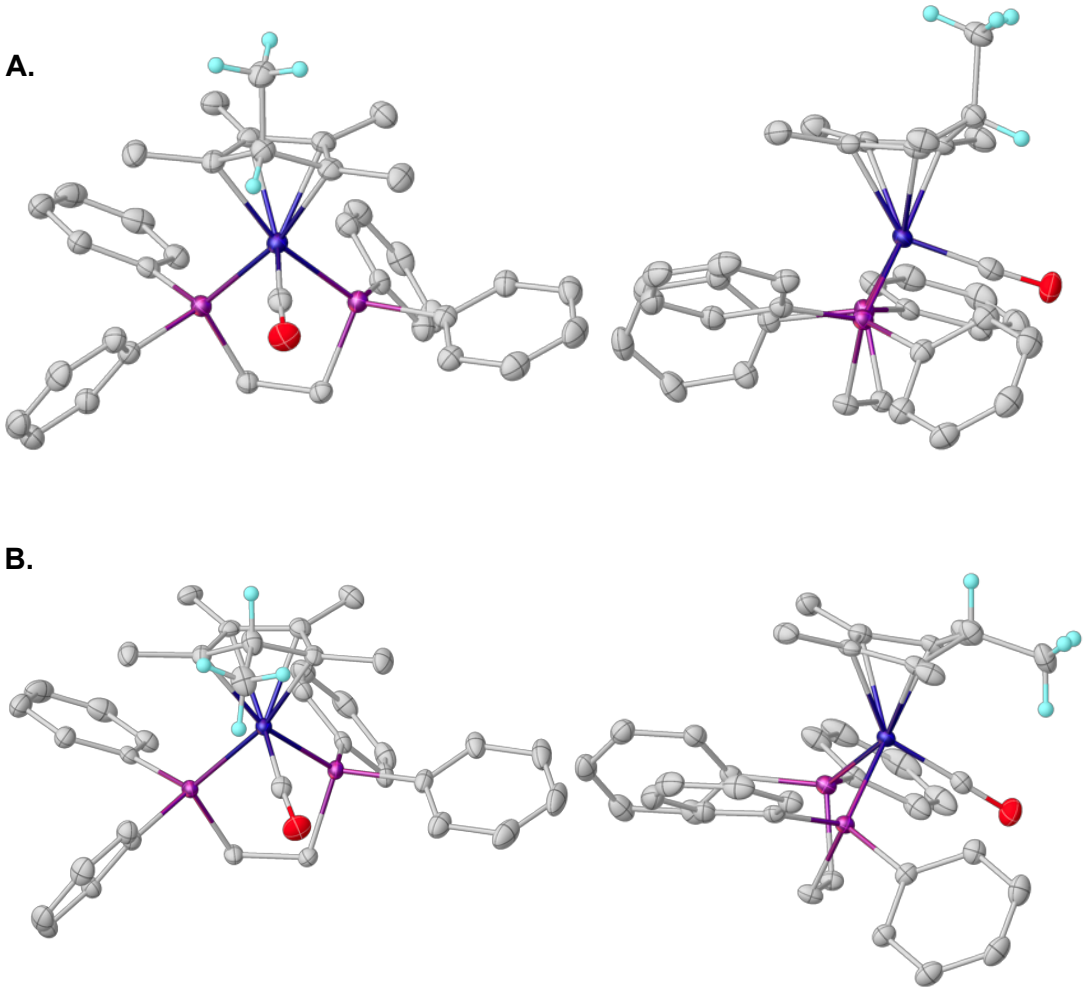

Figure S58. *endo*-[**3**]BAr^{F}_{4}, Thermal ellipsoid plot (50%).

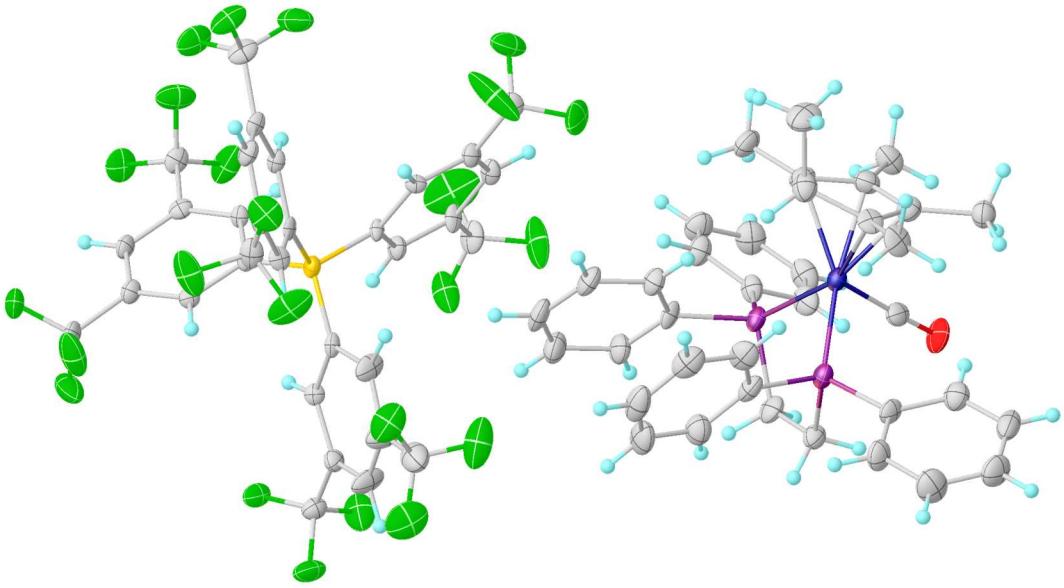

Figure S59. [**6**]BAr^{F}_{4}, Thermal ellipsoid plot (50%, hydrogens omitted for clarity).

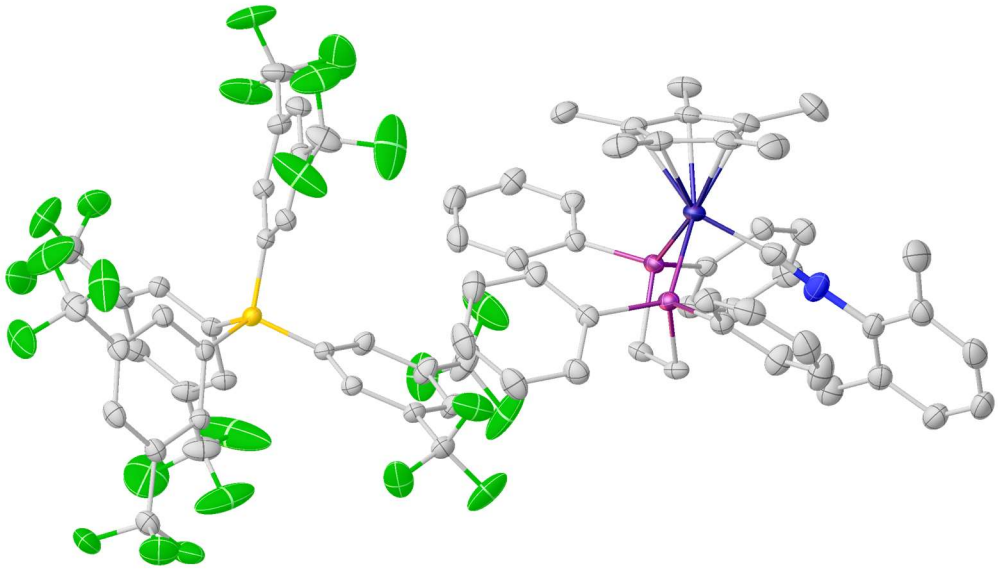

Figure S60. [**7**]$BAr^{F}{}_{4}$, Thermal ellipsoid plot (50%, hydrogens omitted for clarity).

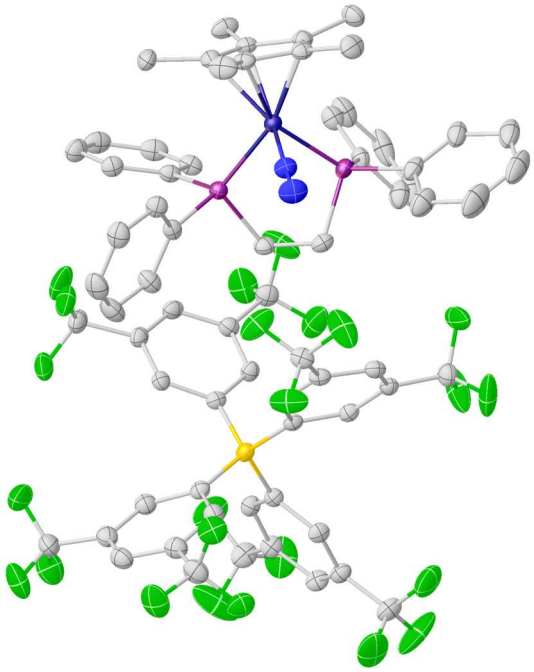

5. DFT Calculations

5.1 General:

All calculations were performed using the ORCA 4.0[10,11] program. In cases where crystal structures were available these coordinates were used as the input. The calculations were performed using the TPSS (meta-GGA)[12] functional with the def2-SVP basis set was on C and H and the def2-TZVP basis set on Fe.[13] To assure that optimized structures represented true stationary points was checked by doing a single-point frequency calculations on the optimized structure.

EPR parameters were calculated using, TPPSh, TPSS, B3LYP, M06L and BP86 with for the TPSS-optimized structure were calculated by doing a single point calculation on the optimized structures using CP(PPP)[14] on Fe and IGLO-III[15] on everything else grid 7. The results were very similar. Thus the EPR parameters were also calculated using CP(PPP) on Co and def2-TZVP on C and H with TPSS, BP86, and B3LYP. Lastly, the EPR parameters for the structures optimized using TPSSh, BP86, and B3LYP were all calculated via a single point calculation using TPSSh with CP(PPP) on Co and Fe and def2-TZVP on C and H with Grid7. See below for a summary of the results.

5.2 $BDFE_{X\text{-}H}$ Calculations:

Consistent with a previous report, a calibration curve of ΔG vs. $BDFE_{lit}$ was employed.[16] The free-energy difference between the H-atom donor/acceptor pair was calculated based on the thermochemical information provided by frequency calculations after structure optimizations using the procedure described in the general computational section.

5.3 EPR predictions

Table S5. EPR parameters of [**1**]$^+$ with different functionals and basis sets. Although a_{iso} varies significantly between the methods, T(^{1}H) remains constant and is characteristic for iron hydrides.

Functional	**Basis set**	**^{1}H (a_{iso}) (MHz)**	**A(^{1}H) (MHz)**	**T(^{1}H) MHz)**
experimental		±36.7	[-10, 60, 60]	[-46.7, 23.3 23.3]
TPSSh	EPR-III (C & H) IGLO-III (P)	-66.34	[-19.33 -83.31 -85.15]	[43.23, -22.55, -20.67]
TPSSh	IGLO-III	-62.59	[-23.11, -88.89, 87.01]	[43.26, -20.72, -22.54]
TPSS	EPR-III (C & H) IGLO-III (P)	-42.33	[-3.85, -62.55, -60.59]	[38.48, -20.22, -18.26]
TPSS	IGLO-III	-39.72	[-1.21, -59.92, -58.02]	[38.51, -20.20, -18.30]
B3LYP	IGLO-III	-81.68	[-36.01, -105.51, -103.51]	[45.67, -23.83, -21.83]
BP86	IGLO-III	-34.39	[2.68, -54.06, -51.78]	[37.07, -19.67, -17.39]
M06l	IGLO-III	-49.08	[-4.69, -72.89, -69.67]	[44.39, -23.81, -20.59]

Table S6. EPR parameters of *endo*-[**3**]$^+$ with different functionals and basis sets. Although a_{iso} varies significantly between the methods, T(^{1}H) remains constant and the small anisotropy is characteristic for ring functionalized (and not metal-hydride) species.

Functional	Basis set	^{1}H (a_{iso}) (MHz)	A(^{1}H) (MHz)	T(^{1}H) (MHz)
experimental		±23.33	[34, 16, 20]	[10.67, -7.33, -3.33]
TPSSh	IGLO-III	25.16	[33.11, 19.93, 22.43]	[7.95, -5.23, -2.73]
TPSS	IGLO-III	26.52	[34.11, 21.34, 24.1]	[7.59, -5.17, -2.42]
B3LYP	IGLO-III	24.24	[32.39, 18.89, 21.42]	[8.16, -5.34, -2.81]
BP86	IGLO-III	23.96	[33.6, 20.81, 23.96]	[7.48, -5.31, -2.16]
M06l	IGLO-III	20.85	[29.43, 15.27, 17.86]	[8.58, -5.58, -2.99]

Table S7. Calculated energies and isotropic ^{1}H hyperfine coupling for rotational isomers of *exo*-[**3**]$^+$ around the Fe-Cp*H centroid axis.

C-Fe-Centroid-C Dihedral Angle (°)	ΔG (kcal/mol)	^{1}H (a_{iso}) (MHz)	A(^{1}H) (MHz)	T(^{1}H) (MHz)
-53.25	0	92.27	[95.44, 91.12, 90.25]	[3.17, -1.15, -2.02]
19	0.446322	43.24	[45.81, 41.67, 42.24]	[2.57, -1.57, -1.00]
89.36	1.098098	63.07	[66.46, 61.83, 60.92]	[3.39.-1.24, -2.15]
-170.03	2.108162	86.32	[81.02, 86.88, 91.05]	[-5,30, 0.56, 4.73]

Figure S61. DFT-optimized structures showing experimental and predicted A(^{1}H) values

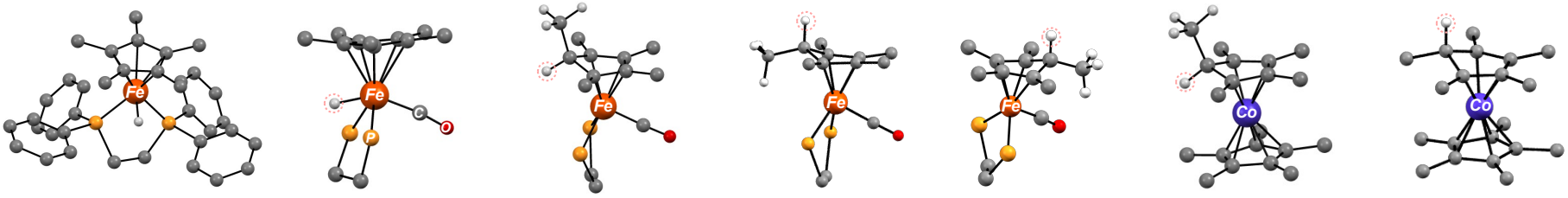

[Fe^{III}(η^5-Cp*)(dppe)(H)]$^+$	[Fe^{III}(η^5-Cp*)(dppe)(CO)(H)]$^+$	[Fe^{I}(*endo*-η^4-Cp*H)(dppe)]$^+$	[Fe^{I}(*exo*-η^4-Cp*H)(dppe)]$^+$ A	[Fe^{I}(*exo*-η^4-Cp*H)(dppe)]$^+$ B	[Cp*(*endo*-η^4-Cp*H)Co]$^+$	[Cp*(*exo*-η^4-Cp*H)Co]$^+$
g = [2.352, 2.041, 1.992]	- -	*g* = [2.083, 2.037, 2.003]	*g* = [2.116 2.073 1.997]	*g* = [2.093 2.035, 2.0012]	*g* = [2.626, 2.349, 1.984]	*g* = [2.170, 2.085, 2.005]
$A(^{31}P_1)$ = ± [88, 82, 79] MHz $A(^{31}P_2)$ = ± [82, 71, 76] MHz	- - - -	$A(^{31}P_1)$ = ± [73, 60, 49] MHz $A(^{31}P_2)$ = ± [49, 51, 49] MHz	$A(^{31}P_1)$ = ± [86, 84, 87] MHz $A(^{31}P_2)$ = ± [78, 75, 63] MHz	$A(^{31}P_1)$ = ± [46, 44, 15] MHz $A(^{31}P_2)$ = ± [70, 64, 64] MHz	- - - -	- - - -
$A(^1H)$ = ± [4, 68, 50] MHz **$a_{iso}(^1H)$ = ± 40.7 MHz** **$T(^1H)$ = ± [-36.7, 27.3, 9.3] MHz**	- - - - - -	$A(^1H)$ = ± [20, 16, 34] MHz **$a_{iso}(^1H)$ = ± 23.3 MHz** **$T(^1H)$ = ± [-3.3, -7.3, 10.7] MHz**	$A(^1H)$ = ± [85, 84, 83] MHz **$a_{iso}(^1H)$ = ± 84.0 MHz** **$T(^1H)$ = ± [1, 0, -1] MHz**	$A(^1H)$ = ± [76 74 70] MHz **$a_{iso}(^1H)$ = ± 73 MHz** **$T(^1H)$ = ± [2 1 3] MHz**	$A(^1H)$ = ± [19.0, 15.0, 19.5] MHz **$a_{iso}(^1H)$ = ± 17.8 MHz** **$T(^1H)$ = ± [1.2, -2.8, 1.7] MHz**	$A(^1H)$ = ± [106.5 112.5, 108.2] MHz **$a_{iso}(^1H)$ = ± 109.1 MHz** **$T(^1H)$ = ± [-2.6, 3.4, -0.9] MHz**
DFT $A(^1H)$ = [-1.2, -59.9, -58.0] MHz **$a_{iso}(^1H)$ = - 39.7 MHz** **$T(^1H)$ = [38.5, -20.2, -18.3] MHz**	$A(^1H)$ = [31.9, 29.2, -70.2] MHz **$a_{iso}(^1H)$ = 43.8 MHz** **$T(^1H)$ = [-11.9, -14.9, 26.4] MHz**	$A(^1H)$ = [24.1, 21.4, 34.1] MHz **$a_{iso}(^1H)$ = 26.5 MHz** **$T(^1H)$ = [-2.4, -5.2, 7.6] MHz**	$A(^1H)$ = [81.0, 86.9, 91.0] MHz **$a_{iso}(^1H)$ = 86.3 MHz** **$T(^1H)$ = [4.7, 0.5, -5.3] MHz**	$A(^1H)$ = [66.4, 61.8 60.9] MHz **$a_{iso}(^1H)$ = 63.1 MHz** **$T(^1H)$ = [3.3, -1.3, -2.2] MHz**	$A(^1H)$ = [30.8 27.9 41.4] MHz **$a_{iso}(^1H)$ = 33.4 MHz** **$T(^1H)$ =[-2.6, -5.5, 8.0] MHz**	$A(^1H)$ = [116.6, 122,5, 117.7] MHz **$a_{iso}(^1H)$ = 118.9 MHz** **$T(^1H)$ = [-2.3, 3.6, -1.2] MHz**

6. Square Scheme:

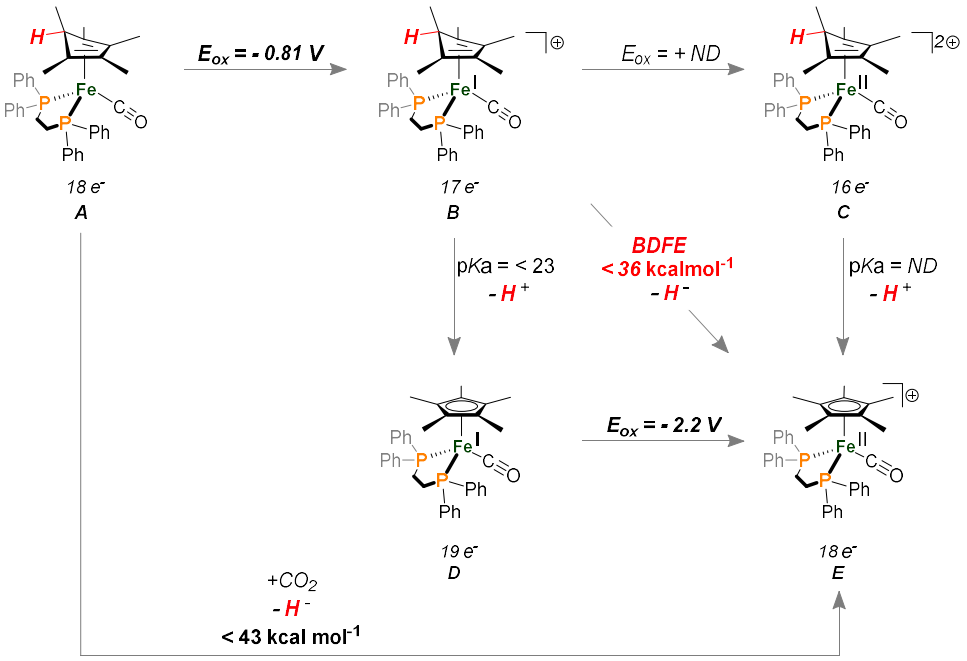

$$BDFE_{(C\text{-}H)} = 1.37pK_a(\mathbf{B}) + 23.06E_{ox}(\mathbf{D}) + 53.6$$

$$BDFE_{(C\text{-}H)} = 1.37pK_a(\mathbf{C}) + 23.06E_{ox}(\mathbf{B}) + 53.6$$

$$BDFE_{(C\text{-}H)} = \Delta G_{(H\text{-})}(\mathbf{A}) - 23.06E_{ox}(\mathbf{A}) - 26$$

Figure S62 Thermochemical scheme relating H+, H•, and H− transfers for *endo*-[**3**]⁺. The oxidation potential of **B** and the p*K*a of **C** could not be determined due to the low stability of the species involved. The upper limit for the p*Ka* of **B** was estimated using the experimentally determined upper limit of the BDFE of **B** and reduction potential of **E**.

7. References:

[1] a) Patel, D.; Wooles, A.; Cornish, A. D.; Steven, L.; Davies, E. S.; Evans, D. J.; McMaster, J.; Lewis, W.; Blake, A.J.; Liddle S.T. Synthesis and characterisation of halide, separated ion pair, and hydride cyclopentadienyl iron bis(diphenylphosphino)ethane derivatives, *Dalton Trans.*, **2015**, 44, 14159–14177 b) Roger, C.; Hamon, P.; Toupet, L.; Rabaa, H.; Saillard, J.-Y.; Hamon, J. R.; Lapinte, C. Halo- and alkyl(pentamethylcyclopentadienyl)[1,2bis(diphenylphosphino)ethane]iron(III) 17-electron complexes: synthesis, NMR and magnetic properties and EHMO calculations. *Organometallics* **1991**, *10*, 1045. c) Hamon, P.; Toupet, L.; Roisnel, T..; Hamon, J. R.; Lapinte, C. Preparation and Characterization of the Triflate Complex [Cp*(dppe)FeOSO$_2$CF$_3$]: A Convenient Access to Labile Five- and Six-Coordinate Iron(I) and Iron(II) Complexes, *European Journal of Inorganic Chemistry*, **2019**, 84

[2] Prisecaru, I. *WMOSS4 Mössbauer Spectral Analysis Software, www.wmoss.org, 2009-2016.*

[3] Stoll, S.; Schweiger, A. EasySpin, a comprehensive software package for spectral simulation and analysis in EPR. *J. Magn. Reson*. 2006, *178*, 42.

[4] Hamon, P.; Toupet, L.; Hamon, J. R.; Lapinte, C. Novel diamagnetic and paramagnetic iron(II), iron(III), and iron(IV) classical and nonclassical hyrides. X-ray crystal structure of [Fe(C$_5$Me$_5$)(dppe)D]PF$_6$. *Organometallics* **1992**, *11*, 1429.

[5] Hamon, P.; Hamon, J. R.; Lapinte, C. Isolation and characterization of a cationic 19-electron iron(III) hydride complex; electron transfer induced hydride migration by carbon monoxide at an iron(III) centre. *J. Chem. Soc. Chem. Commun.* **1992**, 1602.

[6] Paul, F.; Toupet, L.; Roisnel, T.; Hamon, P.; Lapinte, C. Solid-state characterization of the [(η^2-dppe)(η^5-C$_5$Me$_5$)FeCO]$^+$ cation: an unexpected oxidation' product of the [(η^2-dppe)(η^5-C$_5$M$_{e5}$)FeC≡C(C$_6$H$_4$)NMe$_2$]+ radical cation. *C. R. Chim.* 2005, 1174; Catheline, D.; Astruc, D. Synthesis and characterization of C$_5$(CH$_3$)$_5$Fe(CO)$_3^+$ PF$_6^-$ and C$_5$(CH$_3$)$_5$Fe(CO)$_2^-$K$^+$ ***J.*** *Organomet. Chem.* 1982, *226*, c52.

[7] Similar behavior has been noted: a) Zhang, F.; Xu, X.; Zhao, Y.; Jia, J.; Tung, C. –H.; Wang, W. Solvent Effects on Hydride Transfer from Cp*(P-P)FeH to BNA$^+$ Cation**.** *Organometallics* **2017**, *36*, 1238; b) Zhang, F.; Jia, J.; Dong, S.; Wang, W.; Tung, C. –H. Hydride Transfer from Iron(II) Hydride Compounds to NAD(P)$^+$ Analogues. *Organometallics* **2016**, *35* 1151.

[8] Sheldrick, G. M.; A short history of *SHELX*. IUCr. *Acta Crystallogr., Sect. A: Found. Crystallogr.* **2008**, *64*, 112.

[9] Dolomanov, O. V.; Bourhis, L. J.; Gildea, R. J.; Howard, J. A. K.; Puschmann, H. *OLEX2*: a complete structure solution, refinement and analysis program. *J. Appl. Crystallogr.* **2009**, *42*, 339.

[10] Neese, F. The ORCA program system. *Wiley Interdiscip. Rev.: Comput. Mol. Sci.* **2012**, *2*, 73.

[11] Neese, F. Software update: the ORCA program system, version 4.0. *Wiley Interdiscip. Rev.: Comput. Mol. Sci.* **2018**, *8*, 1327.

[12] Tao, J.; Perdew, J. P.; Staroverov, V. N.; Scuseria, G. E. Climbing the density functional ladder: nonempirical meta-generalized gradient approximation designed for molecules and solids. *Phys. Rev. Lett.* **2003**, *91*, 146401.

[13]Weigend, F.; Ahlrichs, R. Balanced basis sets of split valence, triple zeta valence and quadruple zeta valence quality for H to Rn: design and assessment of accuracy. *Phys. Chem. Chem. Phys.* **2005**, *7*, 3297.

[14] Neese, F. Prediction and interpretation of the [57]Fe isomer shift in Mössbauer spectra by density functional theory. *Inorg. Chim. Acta* **2002**, *337*, 181.

[15] Kutzelnigg, Werner, Fleischer, Ulrich, Schindler, Michael. The IGLO-Method: Ab-initio Calculation and Interpretation of NMR Chemical Shifts and Magnetic Susceptibilities in 'Deuterium and Shift Calculation' ed. Maryvonne L. Martin, Gérard J. Martin, NMR Basic Principles and Progress, *16*, 165-262

[16] Matson, B. D.; Peters, J. C. *ACS Catal.* **2018**, *8*, 1448.